

# **Electron beam-powder bed fusion of Alloy 718:**

## **Effect of process parameters on microstructure evolution**

Paria Karimi









# **Electron beam-powder bed fusion of Alloy 718:**

## **Effect of process parameters on microstructure evolution**

Paria Karimi

University West  
SE-46186 Trollhättan  
Sweden  
+46 520 22 30 00  
[www.hv.se](http://www.hv.se)

© Paria Karimi 2020  
ISBN 978-91-88847-65-2 (Printed version)  
ISBN 978-91-88847-64-5 (Electronic version)

*This dissertation is dedicated to; My beloved husband **Esmacil**, for your friendship, love, patience, and endless support, and to my two-month-old sweet girl **Viona**, as you brought us extreme happiness,*

*“You two are my strength in everything I do”*

*My parents who taught me to follow my goals and catch my dreams and be ambitious in life.*

*My brother and sisters for their encouragement in my whole life to success.*



## Acknowledgements

First and foremost, I would like to express my sincere gratitude to my wonderful supervisors at University West, Assoc. Prof. Joel Andersson, and Dr. Joakim Ålgårdh who gave me their consistent support, guidance, encouragement, and constructive suggestions. Thanks for always letting me find my own way in the research track by your trust. I could not have imagined having better advisors and mentors for my PhD study. “*Sky is no limit*” says Joel for any of my requests and I will never forget your trust and positive attitude in encouraging me during my PhD work. “*Excellent work*” or similar phrases as a comment in the review of my papers from Joakim was always making me to be proud of the work.

Besides my supervisors, I will forever be thankful to Prof. Per Nylén, who provided me an opportunity to join production technology center at University West as a PhD candidate. Thank you for giving me the opportunity to be a part of the Additive Manufacturing group at University West. Thanks for your trust on my ambitions and for your “*Wonderful*” word in your replies to my ideas, which was a star in my eyes. I will never forget your collaboration with Esmail to surprise me by selecting me as a Global Swede (One of the biggest achievements in my life, which powdered me to follow my goals): unforgettable!

I would like to appreciate our skilled engineers Mr. Jonas Olsson, Mr. Mats Högström, and Mr. Kenneth Andersson because of sharing their valuable knowledge of additive manufacturing and material characterization. Assoc. Prof. Magnus Hörnqvist Colliander and Dr. Stefan Gustafsson from Chalmers University are highly appreciated for their valuable knowledge in advanced material characterization.

Prof. Ehsan Toyserkani is greatly acknowledged for hosting me at University of Waterloo during my PhD internship. That was an amazing experience working with your PhD students Ali Keshavarzkermani, Reza Esmailizadeh. As well as Asst. Prof. Mihaela Vlasea is appreciated for her kind support and great discussions on my research topic during my stay. Henry Ma from Waterloo University, Dr. Carmen Andrei, and Mr. Jhoynner Martinez from McMaster University are highly appreciated for their great support in the advanced characterization.

I am grateful to my great master students, Bengt Gustafsson (KTH University) and Christopher Schnur (University West) who both did a great job during their periods of study.

Dr. Anders Snis from Arcam-EBM, and Dr. Peter Harlin from Sandvik AB are highly acknowledged for the fruitful discussions on different topics of additive manufacturing and related joint works.

I would like to take the chance and acknowledge Prof. Amir Rashid (who was my opponent in the Mid Seminar before the Licentiate and also my opponent in the Final Seminar before the final dissertation). Prof. Iain Todd (University of Sheffield) as the opponent in the final dissertation, and Assoc. Prof. Fang Liu (Chalmers University), Prof. Lars-Erik Ränner, and Prof. Robert Pederson who will be the members in the examination board are particularly acknowledged. It will be my great pleasure to discuss with you my subject of study and receive invaluable feedbacks from you all.

Eva Bränneby and Victoria Sjöstedt are warmly acknowledged for their administrative support. I also extend thanks to all my delightful colleagues at the Division of welding for their friendship and the pleasant times that we have had together.

I express my gratitude to my friends at PTC for their kind companionship and providing a friendly environment for research. Tayo, Tahira, Vahid, Ali, Amir, Gökce, Magnus, Erik, Oscar, Mohit, Thomas, Pradip, Suhas, Fabian, Satyapal, Ashish, Sneha, Wellington, Karthikeyan, Kaveh, Yongcui, Chamara, Sukhdeep, Arun, Josefine, Agnieszka, Asun, Ana, Anna, Nages, Andreas, and Xiaoxiao; I wish you all the best in your future career!

I would like to thank the financial support received from Innovatum, the “Sustainable Manufacturing Through Next-Generation Additive Process” (SUMAN-Next) projects with funding from the KK foundation, and the support from the research school of Simulation and Control of Material affecting processes (SiCoMap).

Finally, I devote my ultimate appreciation to my husband, Esmail who was my great advisor in PhD work. Your word: “***Your power is more than what you think***” was encouraging me all the time. My cute and sweet angle with her presence in our life was giving me super energy during finalizing my PhD work, thank you my dearest. My wonderful parents, and my sisters and brother are extremely acknowledged for their care, love, and encouragement in my life.

*Paria Karimi*

*1<sup>st</sup> of December 2020, Trollhättan*

## Populärvetenskaplig Sammanfattning

*Nyckelord:* Additiv tillverkning; Elektronstrålesmältning; Mikrostrukturutveckling; Processförståelse, Legering 718

Additiv tillverkning (engelska Additive Manufacturing, AM) är tekniken för att bygga tredimensionella geometrier genom att addera material lager-på-lager till färdig produkt. Av alla de typer av AM-tekniker som idag existerar så har pulverbädd med elektronstrålesmältning (EB-PBF) använts i detta forskningsarbete. Med EB-PBF så kan man producera delar genom selektiv smältning av metallpulver med hjälp av en energität elektronstråle som energikälla. Jämfört med konventionella tillverkningsprocesser erbjuder EB-PBF förbättrad effektivitet för att producera skraddarsydda och specifika produkter inom flyg-, rymd-, fordon- och medicintekniska områden. Dessutom används EB-PBF-processen för att producera komplexa produkter med mindre restspänning i jämförelse med andra AM-processer vilket möjliggörs av den höga byggtemperaturen.

Denna avhandling har delats upp i fyra steg. I det första steget undersöks inverkan hos legering 718 under EB-PBF-processen av olika geometri-relaterade parametrar genom att bygga enkelsträngar intill varandra samt väggar. I detta steg ligger fokus på att förstå effekten av successiv termisk cykling på mikrostrukturell nivå. I det andra steget undersöks de positionsrelaterade parametrarna inklusive avstånd mellan prover, höjd och provplats på byggplattan med avseende på mikrostrukturell inverkan. Det har visat sig att dessa tre positionsrelaterade parametrar kan ha betydande effekt på defektinnehåll samt andelen niob-anrika strukturbeståndsdelar. I det tredje steget har samverkan mellan de viktigaste maskinrelaterade och geometriska parametrarna (smältans bredd, höjd på sträng, återuppsmält djup och kontaktvinkel) och dess inverkan på mikrostruktur (kornstruktur, niob-anrika strukturbeståndsdelar samt primärt dendritarmsavstånd) undersökts. Ovan resultat användes som en riktlinje för att minska olika typer av defekter samt till att kontrollera kolumnär-till-likaxlig kornutväxt. I det sista steget utvecklades två olika strategier med maskinrelaterade parametrar (smälthastighet, strömstyrka, fokusförskjutning, linjeförskjutning och smältstrategi) för att skraddarsy kornstrukturen.

Alla de undersökta parametrarna hade en kritisk roll för att kontrollera den termisk gradienten och kylningshastigheten i stelningsfronten, vilket kunde användas för att erhålla mer likaxliga korn.



## Abstract

*Title:* Electron beam-powder bed fusion of Alloy 718: Effect of process parameters on microstructure evolution

*Keywords:* Additive manufacturing; Electron beam-powder bed fusion; Microstructure evolution; Microstructure tailoring; Process understanding; Alloy 718

*ISBN:* Printed: 978-91-88847-65-2 Electronic: 978-91-88847-64-5

Additive manufacturing (AM) is the technology of building 3D parts through layer-by-layer addition of material. Of the different types of AM techniques, electron beam-powder bed fusion (EB-PBF) has been used in this study. EB-PBF can build parts by melting metallic powders using an electron beam as the energy source. Compared to conventional manufacturing processes, EB-PBF offers a convenient approach and enhanced efficiency in producing customized and specific parts in the aerospace, space, automotive, and medical fields. In addition, the EB-PBF process is used to produce complex parts with less residual stress due to the high-temperature environment within the process.

This thesis has been divided into four stages. In the first stage, the behavior of Alloy 718 during the EB-PBF process as a function of different geometry-related parameters is examined by building single tracks adjacent to each other (track-by-track) and single tracks on top of each other (single-wall samples). In this stage, the focus is on understanding the effect of successive thermal cycling on microstructural evolution. In the second stage, the effect of the position-related parameters—including the distance or gap between samples, height from the build plate (in the Z direction), and sample location on the build plate (in the X–Y plane)—on the microstructural characteristics, are revealed. These three position-related parameters can have significant effects on the defect content and niobium-rich phase fraction. In the third stage, the correlations between the main machine-related parameters, geometric (melt pool width, track height, remelted depth, and contact angle), and microstructural (grain structure, niobium-rich phase fraction, and primary dendrite arm spacing) characteristics of a single track are delineated. The results obtained in stages one to three were used as a guideline for the reduction of the internal–external defects and columnar-to-equiaxed transition (CET) in the grain structure of a typical cubic part. The final stage reveals two different strategies that were developed using machine-related parameters (scanning speed, beam current, focus offset, line offset, and line order number) to tailor the grain structures. All investigated parameters with respect to the proper selection of the processing window played a critical role in the solidification parameters (thermal gradient, growth rate, and cooling rate) on the solidification front, which could induce formation of more fine equiaxed grains.



## Appended Publications

This thesis is written based on the following appended publications:

### Paper A.

#### **Microstructure development in track-by-track melting of EBM-manufactured Alloy 718**

Paria Karimi, Dunyong Deng, Esmaeil Sadeghi, Jonas Olsson, Joakim Ålgårdh, Joel Andersson

Proceedings of the 9<sup>th</sup> International Symposium on Superalloy 718 & Derivatives, 3-6 June 2018; Pittsburgh, Pennsylvania, USA

### Paper B.

#### **Influence of successive thermal cycling on microstructure evolution of EBM-manufactured Alloy 718 in track-by-track and layer-by-layer design**

Paria Karimi, Esmaeil Sadeghi, Pia Åkerfeldt, Joakim Ålgårdh, Joel Andersson

Journal of Materials and Design, Vol. 160, pp. 427-44, 2018; doi.org/10.1016/j.matdes.2018.09.038

### Paper C.

#### **Influence of build layout and orientation on microstructural characteristics of electron beam melted Alloy 718**

Paria Karimi, Esmaeil Sadeghi, Dunyong Deng, Hans Gruber, Joel Andersson, Per Nylén

Journal of Advanced manufacturing technology, Vol. 99, pp. 2903-2913, 2018; doi.org/10.1007/s00170-018-2621-6

### Paper D.

#### **Effect of build location on microstructural characteristics and corrosion behavior of EB-PBF built Alloy 718**

Paria Karimi, Esmaeil Sadeghi, Joakim Ålgårdh, Peter Harlin, Joel Andersson

Journal of Advanced manufacturing technology, Vol. 106, pp. 3597-3607, 2020; doi.org/10.1007/s00170-019-04859-9

### Paper E.

#### **EBM-manufactured single tracks of Alloy 718: Influence of energy input and focus offset on geometrical and microstructural characteristics**

Paria Karimi, Esmaeil Sadeghi, Joakim Ålgårdh, Joel Andersson

Journal of Materials Characterization, Vol. 148, pp. 88-99, 2019; doi.org/10.1016/j.matchar.2018.11.033

**Paper F.**

**Contour design to improve topographical and microstructural characteristics of Alloy 718 manufactured by electron beam-powder bed fusion technique**

Paria Karimi, Christopher Schnur, Esmail Sadeghi, Joel Andersson  
Journal of Additive Manufacturing, Vol. 32, pp. 101014, 2020; doi.  
10.1016/j.addma.2019.101014

**Paper G.**

**Columnar-to-equiaxed transition in powder bed fusion via mimicking casting solidification and promoting in-situ recrystallization**

Paria Karimi, Esmail Sadeghi, Joakim Ålgårdh, Chamara Kumara, Ali Keshavarzkermani, Reza Esmailizadeh, Ehsan Toyserkani, and Joel Andersson

Journal of Additive Manufacturing, Under review, 2020

**Paper H.**

**Tailored grain morphology via a novel double melting strategy in electron beam-powder bed fusion**

Paria Karimi, Esmail Sadeghi, Joakim Ålgårdh, Jonas Olsson, Magnus Hörnqvist Colliander, Peter Harlin, Ehsan Toyserkani, Joel Andersson  
Journal of Additive Manufacturing, Under review, 2020

As the main Author, Paria Karimi has performed most of the experimental characterization, analyzed all the results, designed the structure of all articles, and had the main responsibility in writing the articles. Co-authors contributed to formulating concepts and ideas, assisting in advanced characterization of the microstructural characteristics, planning the project, manufacturing, and article editing.

## Related works

The following papers are not appended but relevant to the work presented in this thesis.

- **Influence of laser exposure time and point distance on 75- $\mu$ m-thick layer of selective laser melted Alloy 718**  
Paria Karimi, Tahira Raza, Joel Andersson, Lars-Erik Svensson  
Journal of Advanced manufacturing technology, Vol. 94, pp. 2199–2207, 2018; doi.org/10.1007/s00170-017-1019-1
- **Effect of powder recycling on the fracture behavior of electron beam melted Alloy 718**  
Hans Gruber, Paria Karimi, Eduard Hryha, Lars Nyborg  
Powder Metallurgy Progress, Vol.18, No.1, pp. 40-48, 2018; doi.org/10.1515/pmp-2018-0005
- **Effect of heat treatment and hot isostatic pressing on oxidation behavior of EBM-manufactured Alloy 718**  
Esmail Sadeghi, Paria Karimi, Mohsen Seifi, Joel Andersson,  
EBAM 2018, 11-13 April 2018; Nurnberg, Germany
- **Isothermal oxidation behavior of EBM-additive manufactured Alloy 718**  
Esmail Sadeghi, Paria Karimi, Pimin Zhang, Ru Peng, Joel Andersson, Lars Pejryd, Shrikant Joshi  
Proceedings of the 9<sup>th</sup> International Symposium on Superalloy 718 & Derivatives, 3-6 June 2018; Pittsburgh, Pennsylvania, USA
- **Influence of thermal post treatments on microstructure and oxidation behavior of EBM-manufactured Alloy 718**  
Esmail Sadeghi, Paria Karimi, Soroush Momeni, Mohsen Seifi, Anders Eklund, Joel Andersson  
Journal of Materials Characterization, Vol. 150, pp. 236-251, 2019; doi.org/10.1016/j.matchar.2019.02.016
- **Subsurface grain refinement in powder bed fusion Alloy 718: Surface texture and oxidation performance**  
Esmail Sadeghi, Prabhat Pant, Reza Jafari, Ru Peng, Paria Karimi  
Journal of Materials Characterization; Vol. 168, 2020; doi.org/10.1016/j.matchar.2020.110567

- **Inclusion-induced fatigue crack initiation of a powder bed fusion Alloy 718 with a tailored microstructure**  
Esmail Sadeghi, [Paria Karimi](#), Niklas Israelsson, James Shipley, Tomas Månsson, Thomas Hansson,  
Journal of Additive Manufacturing; Under review, 2020.
  
- **Enhanced high-temperature performance via surface engineering in powder bed fusion of Alloy 718**  
Mobin Alehojat, Reza Jafari, [Paria Karimi](#), Esmail Sadeghi,  
Journal of Surface and Coatings Technology; Under review, 2020.

# Table of Content

Acknowledgements.....	V
Populärvetenskaplig Sammanfattning .....	VII
Abstract .....	IX
Appended Publications .....	XI
Table of Content .....	XV
Abbreviations and nomenclature .....	XVII
<b>1 Introduction.....</b>	<b>1</b>
1.1 Objective and research questions .....	1
1.2 Structure of the thesis.....	3
<b>2 Background and motivation .....</b>	<b>5</b>
2.1 Metal additive manufacturing.....	5
2.1.1 Benefits and limitations of metal AM .....	5
2.1.2 Classification of metal AM technologies.....	6
2.2 Electron beam-powder bed fusion .....	6
2.2.1 Process description.....	7
2.2.2 Process parameters .....	10
2.2.2.1 Geometry- and position-related parameters.....	10
2.2.2.2 Machine-related parameters.....	12
2.3 Alloy 718.....	14
2.3.1 Strengthening mechanisms.....	15
2.4 Alloy 718 in the EB-PBF process .....	16
2.4.1 Material–electron beam interaction .....	16
2.4.2 Melt pool geometry.....	17
2.4.3 Grain structure .....	19
2.4.3.1 Typical grain structure .....	19
2.4.3.2 Melting strategies for grain structure tailoring.....	20
2.4.3.3 Effect of focus offset.....	23
2.4.3.4 Effect of part location.....	23

2.4.3.5	Effect of energy input, preheating, bed type (build plate, and powder).....	24
2.4.3.6	Effect of in situ heat treatment.....	25
2.4.4	Common phases.....	25
2.4.4.1	Phase evolution and influence of process parameters.....	28
2.4.5	Internal and external defects.....	32
2.4.5.1	Internal defects.....	32
2.4.5.2	External defects.....	36
2.4.6	Hardness.....	36
<b>3</b>	<b>Materials and experimental setup.....</b>	<b>39</b>
3.1	Feedstock powder.....	39
3.2	Sample manufacturing setup.....	40
3.3	Metallographic preparation.....	47
3.4	Characterization techniques and measurements.....	48
3.4.1	Light optical microscopy.....	48
3.4.2	Scanning electron microscopy.....	48
3.4.3	Electron backscattered diffraction.....	48
3.4.4	X-ray computed tomography.....	49
3.4.5	Transmission electron microscopy.....	49
3.4.6	Small-angle X-ray scattering.....	49
3.4.7	Hardness test.....	49
3.4.8	Defect measurement.....	49
3.4.9	Quantification of niobium-rich phases.....	50
3.4.10	Primary dendrite arm spacing.....	50
<b>4</b>	<b>Summary of the appended papers.....</b>	<b>51</b>
<b>5</b>	<b>Conclusions.....</b>	<b>59</b>
<b>6</b>	<b>Future research.....</b>	<b>63</b>
	<b>References.....</b>	<b>65</b>
	<b>APPENDED PUBLICATIONS.....</b>	<b>75</b>

## **Abbreviations and nomenclature**

3D: Three-Dimensional

AM: Additive Manufacturing

APB: Anti Phase Boundary

BSE: Backscatter Electron Detector

BCT: Body Centered Tetragonal

CAD: Computer Aided Design

EB-PBF: Electron Beam-Powder Bed Fusion

EBSD: Electron Backscattered Diffraction

EDS: Energy Dispersive Spectroscopy

EDM: Electrical Discharge Machining

FCC: Face Centered Cubic

GBs: Grain Boundaries

L: Layer

LOM: Light Optical Microscopy

PRS: Powder Recovery System

PBF: Powder Bed Fusion

SEM: Scanning Electron Microscopy

SLM: Selective Laser Melting

STC: Successive Thermal Cycling

T: Track

TCP: Topologically Close Packed

TEM: Transmission Electron Microscopy

$\gamma$ : Gamma

$\gamma'$ : Gamma prime

$\gamma''$ : Gamma double prime

$\delta$ : Delta

G: Thermal gradient

R: Solidification rate

$\dot{T}$ : Cooling rate

XCT: X-ray Computed Tomography

SAD: Selected Area Diffraction

# 1 Introduction

Additive manufacturing (AM) technologies have excited the aerospace world owing to their advanced capabilities compared to traditional manufacturing processes [1]. Specifically, AM has undergone a consistent upward trend in utilization in the fabrication of various individual aircraft components. The aerospace AM global market is projected to reach 2.5 billion USD by 2025 [2]. AM is favorable for the aerospace industry because of its reduced raw material usage, which leads to the lower buy-to-fly ratios that are important for commercial air traffic [3]. The potential for lower fuel consumption owing to lighter components that are designed and manufactured through AM technologies results in the valuable benefit of reduced CO<sub>2</sub> emissions for the aerospace industry.

The electron beam-powder bed fusion (EB-PBF) technique is a unique AM process that has the notable potential to reduce material waste through near net shape production and increase the value of manufactured parts [4], [5]. EB-PBF uses an electron beam heat source that is several times more powerful than other heat sources such as lasers. Because of the high-temperature process in EB-PBF, the residual stress in the manufactured parts is minimized. The production rate in EB-PBF is higher than that in laser-based processes that use a single beam because the electron beam moves using magnetic fields, whereas the laser moves using mechanical mirrors. The increased value of EB-PBF manufactured parts originates from their increased quality due to the vacuum environment used during the processing of the material [6], [7]. Moreover, the EB-PBF process is ideal for the direct low-volume manufacturing of complex parts, such as fuel nozzles for the aerospace industry. This process facilitates the customization of parts using computer-aided design (CAD) to design a 3D metal part with complex geometries, which is difficult to attain in other manufacturing technologies, thus providing better performance of parts [6]. The future of EB-PBF is certainly promising, but to fully exploit its advantages and disadvantages, the relationship between process parameters-microstructure-properties needs to be more extensively investigated.

## 1.1 Objective and research questions

An increased understanding of how microstructural features are developed, affected, and tailored by process parameters is of great importance, as this helps in retaining the consistency and repeatability of the EB-PBF process. This research specifically aims to advance the understanding of how Alloy 718 behaves during the

EB-PBF process and how microstructural characteristics (e.g., defects and phases) are affected and evolved by geometry, position, and machine-related parameters. The knowledge obtained can be used to tailor material characteristics for a given application.

The objective of this research was to establish the relationship between the manufacturing process and the microstructure of the EB-PBF of Alloy 718. To address this objective, four different steps were followed. In Step (1), the main goal was to understand the behavior of the material in the EB-PBF process in depth using the Arcam recommended process theme and to fundamentally understand the development and evolution of the microstructure by the addition of tracks that are adjacent and layer upon layer. In Step (2), the effect of position and orientation of the parts on the microstructure was explored. Step (3) revealed the effects of some critical machine-related parameters on the microstructural characteristics including internal and external defects, grains, primary dendrite arm spacing, and phases. After understanding these three steps, the goal of the final Step (4) was to develop convenient approaches by altering critical machine-related parameters for tailoring the microstructure, particularly the grain structure, as shown in Figure 1-1. The overall goal was to find the proper process window in which parts could be built with fewer internal and external defects and develop novel approaches to tailoring the microstructures.

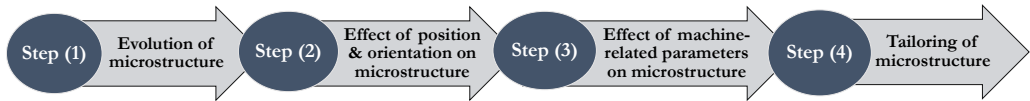


**Figure 1-1: Objective of this research.**

The objective presented in Figure 1-1 could be reached by addressing the research questions (RQs) listed below:

- RQ1: How are the microstructural characteristics of Alloy 718 in the EB-PBF process evolving and what mechanisms are included?
- RQ2: How can the position-related parameters affect the microstructural characteristics of EB-PBF-built Alloy 718?
- RQ3: How can the machine-related parameters affect the internal and external microstructural characteristics of EB-PBF-built Alloy 718?
- RQ4: How can the microstructure of Alloy 718 in EB-PBF process be tailored by altering critical machine-related parameters?

### **1.2 Structure of the thesis**

This thesis consists of six chapters, including this introduction, which briefly describe the framework of this research and the structure of the thesis. Chapter 2 provides the background of metal AM and EB-PBF processes for a better understanding of the main motivation behind this study and why this work is relevant to the scientific community. A comprehensive literature review of the main characteristics of Alloy 718 processed in EB-PBF is discussed in Chapter 2. Chapter 3 describes the experimental procedure and the characterization techniques utilized for the material investigation. Details of the process conditions and the design of the experiments are provided as well. Chapter 4 summarizes the articles published in relation to this work, which are appended to the thesis. Finally, Chapters 5 and 6 present the conclusions and recommendations for future research, respectively.



## 2 Background and motivation

### 2.1 Metal additive manufacturing

The definition of AM, according to the American Society for Testing and Materials (ASTM) International Standard, is as follows:

“The process of joining materials to make objects from 3D-model data, usually layer upon layer, as opposed to subtractive manufacturing methodologies, such as traditional machining” [4], [8].

In general, the goal of metal AM technologies is to produce lighter and stronger metal parts and reduce or eliminate post-processing steps to decrease the overall costs of manufactured parts [9]. Although metal AM is beneficial in terms of design and cost, there is still a long way to go toward understanding complex thermo-physical phenomena such as heat transfer mechanisms, thermal stresses, and phase transformations. All these phenomena significantly affect the quality and properties of the final part. Moreover, owing to the localized, fast, and transient nature of the metal AM process, quantitative experimental measurements are extremely difficult to obtain [10], [11].

#### 2.1.1 Benefits and limitations of metal AM

One of the major benefits of metal AM is its significant potential in the design and manufacturing of complex geometries with specific design-related features without employing a tooling process, the use of which is common in conventional manufacturing processes [12], [13]. In addition, metal AM technologies are considered to be highly favorable for low-volume production, for example, the production of customized single parts [14], [15]. Depending on the demand, the elimination or reduction of post-processing, such as machining, leads to a significant decrease in the production ramp-up time, cost, and waste. For specified parts, shorter lead times, lower inventories, and the integration of multiple parts into one single part can be reached through metal AM. Moreover, metal AM offers the possibility of simultaneously manufacturing multiple individual parts [16], [17]. These benefits make metal AM an interesting alternative in many industries such as aerospace, space, biomedical, and automotive [18].

In contrast, the as-built material characteristics of a part manufactured by metal AM may be influenced by its geometry [19], [20]. Therefore, there is no optimal process setting that fits in all instances. Part orientations, heights, and angles can

influence localized heat concentrations, leading to the formation of defects, phase transformations, and residual stresses [21], [22].

The main disadvantages of parts manufactured by metal AM are a poor surface finish and poor dimensional accuracy. The layer resolution in metal AM produces a staircase appearance on the surface, which is inherent in all metal AM techniques [23]. Currently, some parameters, such as layer thickness or the temperature profile of the melt pool, are controlled to improve the surface finish [24], [25].

Another general drawback of metal AM that is of great importance is related to defects such as pores, shrinkage, lack-of-fusion, cracks, and inclusions, which are difficult to monitor and quantify during manufacturing [18]. Moreover, *in situ* process control is challenging in many metal AM techniques. Online process monitoring has been extensively investigated in metal AM techniques because the material properties are highly dependent on the build history [8], [15], [26], [27].

### 2.1.2 Classification of metal AM technologies

Generally, metal AM techniques can be categorized into three main groups based on the type of feedstock material: i) powder, ii) wire, and c) sheet [6], [28]. Metal AM processes can be categorized based on the heat source as well, that is, i) electron beam, ii) laser beam, and iii) Arc-based. The scope of this study only includes powder bed fusion using an electron beam as the heat source, which will be discussed further. Figure 2-1 briefly illustrates a schematic of the different metal AM techniques.

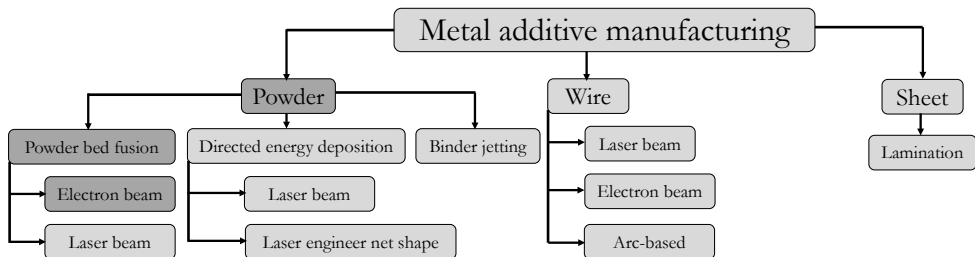


**Figure 2-1: Process overview of metal-based AM technologies, the dark gray color shows the EB-PBF process, modified from [28].**

## 2.2 Electron beam-powder bed fusion

In the EB-PBF process, powder in the bed is selectively sintered and melted using an electron beam as the heat source. Additionally, by melting a layer, the underlying layers are remelted to obtain sufficient adherence to the newly added

## BACKGROUND AND MOTIVATION

layer and to the rest of the part [4]–[6], [29]. The EB-PBF process uses a high-power scanning electron beam and offers a higher build rate than other PBF techniques using the same number of heat sources such as single-beam laser-based techniques [6]. This process was commercialized by a Swedish company called Arcam AB in 1997 [4], [6]. Based on the literature, it has been found that this process can be used for multiple types of high-temperature conductive metallic materials. The most extensive work has been performed for titanium alloys (mainly Ti–6Al–4V) [15], [18], [22], [30]; however, other materials such as intermetallic titanium aluminide [31], nickel- and nickel-iron-based superalloys (Alloy 718, Alloy 625, Rene 142, Haynes 282, Hastelloy X) [6], [27], [32]–[37], copper [38], [39], cobalt-chromium alloys [40], and 316L and H13 steel [41]–[43] have also been investigated for this process.

### 2.2.1 Process description

As shown in Figure 2-2, the electron beam column is located on top of the main chamber of the EB-PBF equipment. The cathode (tungsten filament) and anode are used in this unit to generate an electron flow in the column. The cathode filament is heated by the application of voltage and current to release electrons. The anode must be attached to the ground to create a potential difference between the cathode and anode [29]. Because of the negative electric potential of the cathode with respect to the grounded anode, negatively charged electrons emitted from the cathode see a potential gradient and accelerate towards the anode [44]. Furthermore, three different sets of electromagnetic lenses are located in electron gun chamber: i) astigmatism lenses to produce a circular beam with a Gaussian energy distribution, ii) a focal lens to focus the beam onto a spot of appropriate size as well as focus/defocus the electron beam during the preheating/sintering/melting steps, and iii) a deflection lens to control the beam scan across the build plate. Two powder hoppers are located inside the build chamber. Below the powder hoppers, there is a raking system that distributes the powder from the hoppers by spreading it over the build plate. The build plate, which is placed under the heat shield, is lowered along the Z-axis during the building process.

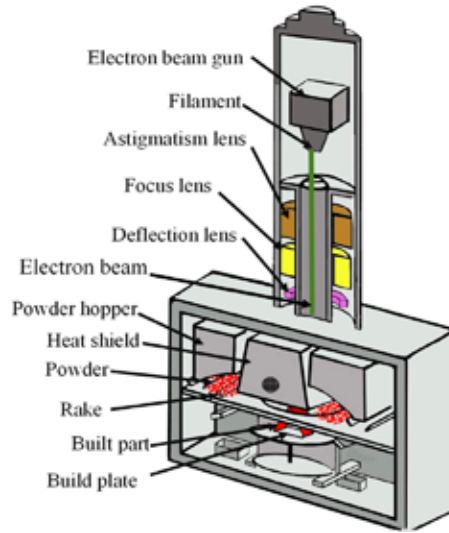


**Figure 2-2: Schematic of the EB-PBF process, including the basic components with the labels.**

A typical EB-PBF process follows the steps below:

- 1- **CAD:** A CAD of the part must be drawn, and a “sliced” CAD model of the part must be transferred to the working memory of the machine.
- 2- **Vacuum pumping:** Vacuum conditions of up to approximately  $10^{-5}$  mbar are provided in the build chamber. In addition, a small amount of inert helium at a partial pressure of approximately  $2 \times 10^{-3}$  mbar is also injected into the vacuum chamber to prevent electrical powder charging and provide thermal stability to the process [6], [45], [46]. A vacuum environment in the e-gun column and building chamber is needed for the following reasons:
  - Avoiding the interaction of electrons with gaseous atoms.
  - Preventing chemical reactions of the elements present in sensitive materials, such as titanium, with atmospheric gases such as oxygen.
  - Acting as an insulator to maintain an elevated process temperature.
- 3- **Preheating #1:** Heating the build plate (typically stainless steel), which also leads to partial sintering of the powder on top of the build plate. The heating temperature is highly dependent on the given material. The temperature for Alloy 718, which is the material investigated in this study, is approximately  $1025^{\circ}\text{C}$ . Heating is accomplished by rapidly scanning a defocused beam over the build plate or powder surface. The elevated temperature helps to reduce the residual stress in the as-built parts.

## BACKGROUND AND MOTIVATION

- 4- **Lowering the build plate:** The build plate usually moves down by between 50 and 200  $\mu\text{m}$ , known as the layer thickness, which is defined by the operator.
- 5- **Raking:** The rake spreads a layer of powder over the build plate.
- 6- **Preheating #2:** This step is mainly performed in the areas on the build plate that are supposed to be fully melted (mainly the areas in which the parts are assumed to be built). The general aim of preheating #2 is to heat the distributed powder layer to the desired sintering temperature. This temperature is approximately 80% of the melting temperature, and a defocused beam scans over the build plate to slightly sinter the powder. The sintering step helps to enhance the conductivity between the individual powder particles and prevents the movement of powder during melting with a focused beam [4], [6], [47].
- 7- **Support/wafer melting (optional):** This step can be carried out in any order relative to preheating #2 and the post-heating steps. Supports are mainly used for two purposes: i) mechanical integrity and ii) thermal support. Mechanical support prevents overhangs from deformation induced by gravity or growth stresses. The thermal supports conduct the applied energy from the melt surface to the build plate.
- 8- **Contour melting:** As shown in Figure 2-3, the border/skin/frame of a part is called the contour and is melted using a multispot strategy to yield the desired surfaces of the final part [48]. Typically, three contours (two inner to increase margins and one outer to control the surface roughness) are run as a frame for the bulk region (see Figure 2-3). There is an overlap between the inner and outer contours and between the inner contour and the bulk region. The optimization of the contour parameters, for example, beam current, spot melt order, overlaps, the order of contours, and the number of contours, is important for determining the surface finish of the as-built parts.
- 9- **Hatch/bulk melting:** The hatch/bulk is the inner region of the part that is scanned. The hatch scan strategy involves linear and continuous melting in which the beam moves back and forth; see Figure 2-3.

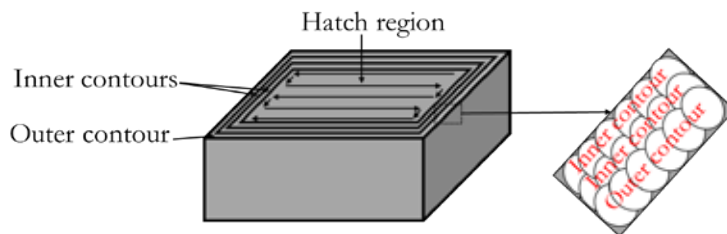


**Figure 2-3: Schematic of contour with the multispot melt strategy and hatch region with the snaking melt strategy.**

- 10- Post-heating:** This step is performed, if needed, after melting all single layers to maintain a constant build temperature. The amount of applied energy in this step depends on the total applied energy in the previous steps (preheating #1 and 2, contour melting, hatch melting, and support) and the target energy (according to the pre-defined heat model) using the average beam current for every single layer.
- 11- Repetition until the final finished part:** Steps 4 to 10 are repeated several times in the newly added layers to complete the entire part [32].
- 12- Cooling:** When the building job is completed, the chamber is cooled from an elevated temperature to below 100 °C. There are two approaches to lowering the temperature in this step— fast cooling and slow cooling. During fast cooling, helium is injected inside the chamber to increase the rate of cooling; however, during slow cooling, the chamber is under vacuum, resulting in a longer cooling time.
- 13- Powder recovery system:** Partially sintered particles are removed from the final part using compressed air and blasting with the same powder particles. Typically, the powder blasted off the part is recycled for future use.

## 2.2.2 Process parameters

In general, the process parameters can be divided into three different categories: i) powder-related, ii) geometry and position-related, and iii) machine-related. In this work, critical parameters related to the geometry and position of the parts on the build plate and key EB-PBF machine-related parameters were investigated. Although parameters related to geometry and position are limited, there are more than a hundred machine-related parameters in the EB-PBF process that can be directly/indirectly altered [48]. Some of the machine-related parameters are changed according to the setting, and some are changed automatically as part of the different process settings. The main critical machine-related parameters are beam scanning speed, beam current, line offset, layer thickness, focus offset, scanning strategy, and line order [49]. The following is a brief description of some important process parameters from the literature that are related to the scope of this research.

### 2.2.2.1 Geometry- and position-related parameters

Geometry-related parameters are linked to the geometry of the part to be built, which considers the thickness of the part in different sections. Investigation of these parameters provided a platform to understand the evolution of the microstructural characteristics in this study (see papers A and B). The position-related parameters are linked to the type of stacking or the orientations of the parts on the build plate. Some of these parameters relevant to this research consist

## BACKGROUND AND MOTIVATION

of the distance between the parts on the build plate, the height of the parts from the build plate, and the location of the parts on the build plate (the exterior or interior locations of the build plate; see papers C and D). A few studies have been found on this research topic [20], [50]–[54], [54]; more research is needed because each of these parameters can have a significant effect on the thermal history of the part, which is the main factor influencing its microstructural evolution. In the following section, a short illustration of these parameters, including part geometry, height from the build plate, location on the build plate, and distance between the parts on the build plate, are presented to better understand their effects on the microstructural characteristics.

- **Part geometry:** Different thicknesses in different sections of a part can have a significant local effect on the microstructures (e.g., texture and morphology of the grains) [19], [55]. It is expected that larger/thicker parts would have higher heat accumulations due to long scan lines, which results in lower cooling rates and coarser microstructures [21].
- **Height from the build plate:** By elevating the parts from the build plate, the powder below the parts affects the thermal conductivity of the parts to the build plate, which subsequently affects the microstructural characteristics. For instance, by increasing the height from the build plate, the cooling rate is reduced, which is due to the accumulation of powder with a lower thermal conductivity beneath the part [21].
- **Location on the build plate:** Another position-related parameter that could affect the microstructural features is the location of the parts on the build plate. The hypothesis that heat is distributed differently depending on the location on the build plate is considered. In this hypothesis, it is assumed that the interior areas of the build plate would be the warmest region, and the temperature would decrease outward towards the exterior areas of the plate. Thus, it is expected that the exterior parts would have finer microstructures and better mechanical properties compared to the parts located in the interior areas [22].
- **Distance between the parts on the build plate:** The distance between individual parts can be used to define two different terms, that is, open design and close design. In a close design, the parts are fairly close to each other, and the distance between them is at least 2 mm (the distance recommended by the EB-PBF machine manufacturer); therefore, greater heat accumulation is expected. Thus, in close design, higher heat accumulation can lead to a lower cooling rate. However, in an open design, with a larger distance between the parts, heat dissipation is assumed to be faster, and accordingly, the cooling rate is higher.

### 2.2.2.2 Machine-related parameters

The effect of critical machine-related parameters on the microstructural features was evaluated in this study (see papers E–H) and are briefly presented here.

- **Beam scanning speed:** The speed of the electron beam is mainly controlled by the deflection coils. According to Eq. 1 [56], the beam scanning speed has an inverse effect on the energy input per volume of material; thus, the speed can have a significant impact on the microstructural characteristics. The scanning speed at the contour and the hatch regions is different owing to the difference in the scanning strategies selected for the two regions. In addition, the beam scanning speed changes slightly along the scan line (X- and Y-axes) and build direction (Z-axis) to maintain energy balance (to maintain a stable heat model) during the EB-PBF process [6], [48], [49], [57], [58]. In fact, the energy balance is ensured by a complex set of process parameters (one of which is the scanning speed) that allows the operator to control the behavior of the beam. The maximum recommended scanning speed in an A2X machine (manufactured by Arcam-EBM) is 8000 mm/s [6].

$$\text{Energy input } \left(\frac{J}{\text{mm}^3}\right) = \frac{\text{Power} = \text{Voltage (kV)} \times \text{Beam current (mA)}}{\text{Scanning speed (mm/s)} \times \text{Line offset } (\mu\text{m}) \times \text{Layer thickness } (\mu\text{m})} \quad (1)$$

- **Beam current:** This parameter has a direct correlation with the energy input (see Eq. 1) and can reach a maximum of 50 mA. Indeed, the relationship between the beam current and scanning speed is highly important in EB-PBF owing to its great effect on the elimination of process-induced defects and the determination of the grain structure [57], [59], [59].
- **Focus offset:** The value of current, in mA, applied to the focusing coil in the e-gun column to generate the sufficient magnetic field to control the beam focal point. Basically, the produced electron beam will diverge after passing through the anode plate from the emission source. By using the focusing coil, the electron beam is converged and collimated into a relatively parallel stream. The position of the focal point can be controlled by adjusting the focusing coil current. In fact, the focus offset significantly affects the geometry of the melted tracks [6], [49] as the focus offset is related to the beam intensity and beam size. Moreover, it must be considered that the focus offset value relates to a relative value that is needed to obtain the optimal spot behavior at a given moment and cannot be stated in absolute values. As shown in Figure 2-4, the beam spot size is affected by the position of the focal point, which can be above the build plate (a), on the build plate (b), or below the build plate (c). The

## BACKGROUND AND MOTIVATION

beam focal point is mainly affected by the applied focus offset and the applied beam current.

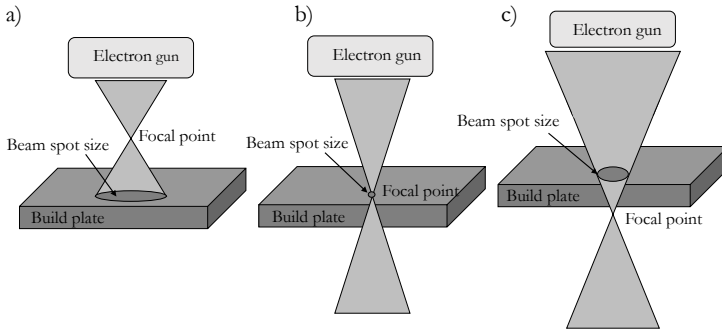


**Figure 2-4: Schematic illustration of the focus offset: a) focal point above the build plate, b) focal point on the build plate, and c) focal point below the build plate.**

- Line offset:** The distance between two adjacent beam scanning passes; see Figure 2-5a. One approach for reducing the content of pores is to optimize the line offset. By decreasing the value of the line offset, the overlap between two adjacent passes can be increased; therefore, there is less risk of the presence of unmelted powder particles in the final part. In contrast, for a higher line offset, the risk of the unmelted powder particles being present at the bottom of the overlapping area can be high, as shown in Figure 2-5b–c [33], [60].

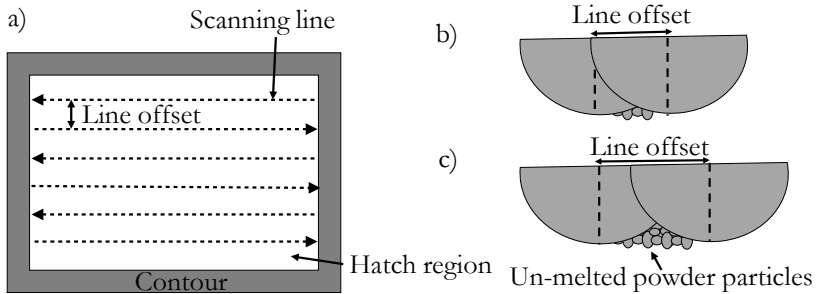


**Figure 2-5: Schematic illustration of a) the line offset, b) the overlapping area with a lower line offset, and c) the overlapping area with a higher line offset.**

- Scanning strategy:** The electron beam path employed during the process is termed the scanning strategy, which can be used as a tool for tailoring the microstructure [61]. The scanning strategy is typically different in the hatch and contour regions. Commonly, multispot melting is used in the contour region; in contrast, different types of scan strategies

can be applied in the hatch region, including unidirectional, bidirectional/snaking, and multispot melting (see Figure 2-6). In the case of a unidirectional or bidirectional/snaking strategy, the rotation of the hatch direction is performed at a pre-defined angle between each layer. In addition, for a specific scanning strategy, the beam scanning speed and current must be optimized [6], [59].

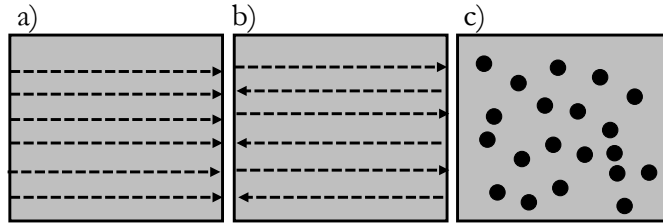


**Figure 2-6: The different scanning strategies used in the EB-PBF process in the XY plane: a) unidirectional, b) bidirectional/snaking, and c) spot melting.**

- Line order number:** This function provides the possibility to melt specific areas in the hatch region according to a pre-defined number. Line order number one means melting the first scan line and jumping to the adjacent scan line for melting (1, 2, 3, and so on). Line order number two means melting the first scan line and jumping to the third one and melting it (1, 3, 5, and so on). Thus, if the line order number is  $n$ , then the melting order for scan lines will be  $1, 1+n, 2+n$ , and so on (see Figure 2-7).

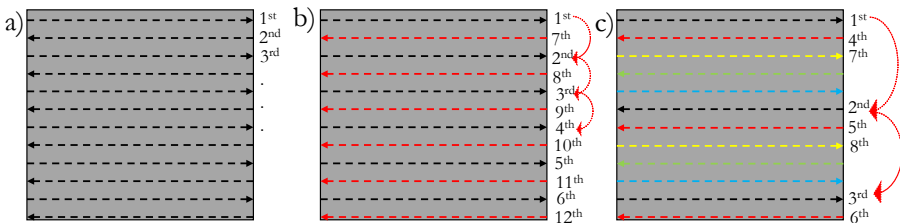


**Figure 2-7: The different line order numbers in the XY plane with bidirectional scan strategy: a) line order number of one, b) line order number of two, and c) line order number of five.**

## 2.3 Alloy 718

The development of Alloy 718 in 1959 as a Ni–Fe-based superalloy was a great achievement owing to its unique properties, the most important of which is the maintained mechanical properties at elevated temperatures (up to 650 °C) under high stresses [62]. It also has reasonably good weldability, is relatively insensitive to strain age cracking, and exhibits good resistance to oxidation and corrosion

[62]–[64]. Based on these properties that reflect the advantages of Alloy 718 compared to other materials, it has been the material of choice for many high-temperature applications, such as gas turbines and rocket engine components, and in low-temperature applications, such as nuclear power plants [64]–[67].

### 2.3.1 Strengthening mechanisms

There are different strengthening mechanisms in Alloy 718: I) solid solution strengthening, II) precipitation strengthening, and III) grain boundary strengthening, which are briefly described here [68].

I) *Solid solution strengthening:* One of the primary strengthening mechanisms in metallic materials involves an element (solute) being dissolved into the lattice of a host metal (solvent, the  $\gamma$  matrix phase) to form a solid solution strengthened alloy that has a strength greater than that of the host metal. The strengthening mechanism is linked to the difference in the atomic radii of the solute and the solvent matrix, which causes distortions in the face-centered cubic (FCC)  $\gamma$  lattice structure. These distortions hinder the dislocation movement in the matrix, thereby strengthening the alloy [26], [63], [68].

II) *Precipitation strengthening:* The main strengthening mechanism in Alloy 718 is the precipitation of the  $\gamma^2$ -Ni<sub>3</sub>(Ti, Al) and  $\gamma''$ -Ni<sub>3</sub>Nb phases, in which the latter has a greater influence. Certain elements with low solubilities in the  $\gamma$  matrix, such as niobium, titanium, and aluminum, must be added to facilitate the formation of these precipitates. Principally, the strengthening effect is obtained by the coherency strain developed between the strengthening precipitates and the matrix. In addition, an antiphase boundary energy is developed that resists dislocation movement between the ordered strengthening phases in the matrix. Furthermore, by increasing the size of the precipitates to a certain level, the precipitation strengthening mechanism becomes more dominant.  $\gamma'$  as a coherent and  $\gamma''$  as a semi-coherent intermetallic compound prohibit the movement of dislocations. The movement of the dislocations in the matrix containing these precipitates can only take place by cutting through or bypassing them [68].

In addition to the main strengthening precipitates in Alloy 718, elements with limited solubility, such as niobium, titanium, and molybdenum, are able to form carbides, such as NbC and TiC, that provide high-temperature strengthening. In general, carbides are preferentially precipitated in the intergranular regions and subsequently in the intragranular regions. A uniform distribution of fine carbides in the microstructure can improve the mechanical properties of the material. The carbides formed at the grain boundaries

prevent grain boundary slip and transfer the deformations to the interior grain regions, where creep diffusion is slower [69], [70].

III) *Grain boundary strengthening*: The reduction in the size of the grains leads to the formation of more grain boundaries, which prevents the movement of dislocations, thus delaying failure and improving the strength of the material. It is well recognized that a fine-grained microstructure displays good tensile properties and toughness as well as improved high-cycle fatigue performance [71].

## **2.4 Alloy 718 in the EB-PBF process**

In this section, the physical phenomena occurring during the material–electron beam interaction are explained. The microstructural features (including the melt pool formation, grains, phases, and defects) and hardness of Alloy 718 in EB-PBF are discussed. The evolution of the microstructural features and approaches to tailoring the microstructure are summarized in this section.

### **2.4.1 Material–electron beam interaction**

The first point in understanding the microstructural evolution is recognizing the interaction between the electron beam and the powder particles, which leads to the formation of melt pools. This interaction consists of various types of physical phenomena occurring at the same time. However, due to the difficulties in capturing them, it will be difficult to understand the influence of individual phenomena. Here, some basic and typical phenomena observed during the interaction are discussed. Sames et al. [72] disclosed two facts as a result of this interaction.

I) Molten jet spattering, which is the convective transport of liquid or vaporized metal out of the melt pool. Molten jet spattering occurs when a high-energy input beam leads to localized boiling. The energy of the spattered molten jets exceeds the surface tension forces, which facilitates the spattering. The spattered particles typically appear as fireworks in EB-PBF, as shown in Figure 2-8a.

II) The electrostatic repulsion of the powder particles or smoking, which is due to electrical charge transfer from the beam to the powder particles. If the gravity and the forces holding the powder particles are lower than the repulsive electrostatic forces, smoking of the powder particles could occur. This can cause bulk displacement of the powder particles in the powder bed. One potential reason for smoking could be the selection of an inappropriate sintering temperature. Smoking can be avoided in EB-PBF by using the right machine-related parameters, such as increasing the line order number or increasing the beam spot size during the sintering step prior to melting. Moreover, the injection

## BACKGROUND AND MOTIVATION

of small quantities of helium during melting to dissipate charge from the melt surface limits smoking (Figure 2-8b).

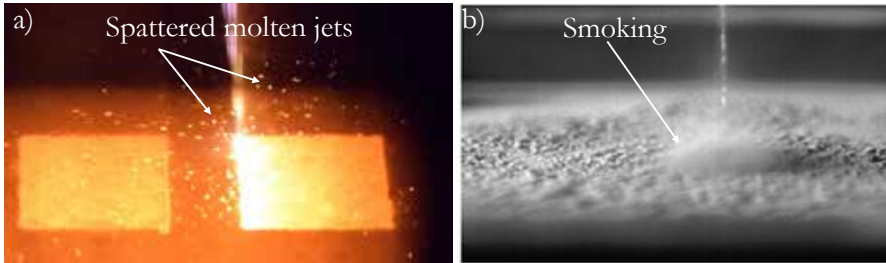


**Figure 2-8: Photos taken from the melting step showing the electron beam-material interaction; a) molten jet spattering and b) smoking [73].**

The type of heat transfer is also a critical factor that influences the material-electron beam interaction, and subsequently, the melt pool geometry as well as the microstructure. Owing to the vacuum environment in EB-PBF, the main type of heat transfer is heat conduction to the machine. Heat radiation is a side loss from the build surface, and heat transfer through convection is significantly limited in the melting process [72]. Different machine-related or geometry-related parameters, such as scanning strategy or part geometry, affect the heat flow rate and type. For instance, when a heat source passes close to an edge, it may return to the same edge before the heat has time to disappear from the previous pass; therefore, the scanning strategy and part geometry can have a critical impact on the cooling process between each melting pass [72].

### 2.4.2 Melt pool geometry

Melt pool geometry is a key factor in determining the solidification mode in the EB-PBF process. One important parameter affecting the melt pool geometry is the scanning speed–beam current relationship, which is defined as the speed function in the EB-PBF machine. This function helps determine the proper scanning speed, based on the beam current, to obtain a dense material. The dynamic scanning speed–beam current relationship is closely related to the material, scanning strategy, layer thickness, and part geometry [6]. Sames et al. [72] reported that the powder has a lower thermal conductivity than the solid material, so the powder has a high impact on the size of the melt pool. It was also observed that if the length-to-diameter ratio in the melt pool was higher than 2.1, the melt pool geometry changed from a weld bead to a melt ball. Theoretically, the melt ball formation is dependent on the surface tension forces, wetting forces onto the underlying layers, and capillary forces. Ding et al. [74] reported that, generally, the width and depth of the melt pools expand almost linearly with the applied line energy input. In a low beam current and at a high scanning speed, the single tracks

were barely distinguishable. By increasing the beam current and decreasing the scanning speed, the single tracks became continuous and stable in the presence of several cracks. It was found that the preheating step played a key role in the geometry of the melt pools. The single tracks built on the build plate using the preheating step contained larger melt pools than those built without preheating. The continuity of the single tracks with preheating was better than that without preheating, probably due to the lower heat input needed in the case of preheating. Furthermore, no cracks were observed in the single tracks built with preheating, mainly due to the lower thermal gradient, which results in lower internal stress. It was reported that the existence of a powder bed beneath the single tracks increased the melt pool size and improved the continuity of the single track, probably due to the low heat conductivity of the powder bed. However, the edge smoothness of the single tracks was lower in this case, owing to the existence of powder particles around the melt pool. The continuity of the single tracks at lower linear energy input using a powder bed was lower than that using a bulk bed owing to strong nonwetting conditions and capillary instability. The capillary and wetting forces depend on the process parameters and are responsible for the formation of the melt balls and droplets at a lower linear energy input. By increasing the linear energy input in a single track on the powder bed, bowl-shaped melt pools were formed. This was probably due to the involvement of a large number of powder particles during melting. During solidification, the apparent volume of the melted area shrinks remarkably, such that there is not enough material to fill the concave space in the remelted track. This results in the formation of bowl-shaped melt pools. The bowl-shaped melt pools lead to the formation of an uneven surface after multiple beam scanning.

The effect of the focus offset on the melt pool geometry was evaluated by Lee et al. [75]. It was reported that by increasing the focus offset, the melt pool geometry became broader and shallower, and finally, the electron beam became so blurry that the powder was not fully melted (see Figure 2-9). In addition, by decreasing the focus offset (smaller spot size), small and deep melt pools were formed, which increased the number of defects.

## BACKGROUND AND MOTIVATION

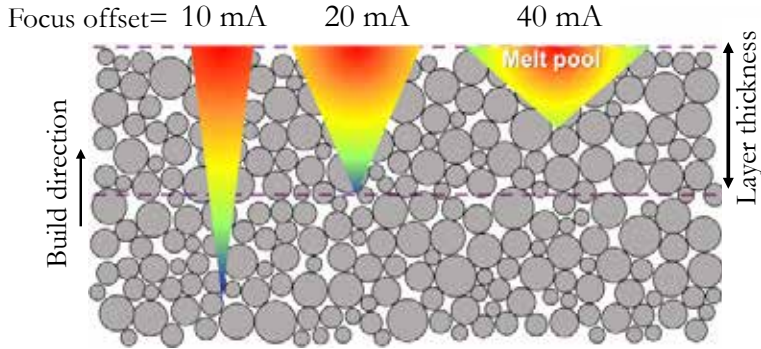


**Figure 2-9: Schematic illustration of the shape and size of the melt pool with respect to focus offset [75].**

### 2.4.3 Grain structure

Conventional manufacturing processes have limitations with respect to controlling and inducing site-specific control over grain size, morphology, and texture. These processes have a weakness in controlling the heat transfer conditions at very small length scales. To obtain the target microstructure for a given application, knowledge of dynamic switching between equiaxed and columnar solidification conditions is highly necessary. This requires extensive trial and error. In this section, some studies related to the scope of this research are briefly discussed.

#### 2.4.3.1 Typical grain structure

The most common grain structure in the as-built EB-PBF parts was reported by Strondl et al. [76], [77] to be columnar grains in the hatch/bulk region, as shown in Figure 2-10a. The presence of elongated columnar grains in the  $\gamma$  matrix was reported. These grains were up to several millimeters in length and up to 1 mm in diameter with a very strong  $\langle 001 \rangle$  texture along the build direction. The grain structure was different in the contour and hatch regions because of the different process conditions in the two regions, as reported by Deng et al. [78]. An inhomogeneous grain morphology was observed in the as-built material, including i) equiaxed grains with a weak texture close to the surface in the contour region, and ii) elongated columnar grains with  $\langle 001 \rangle$  texture parallel to the build direction in the hatch/bulk region, as shown in Figure 2-10b–c. The center part of each contour line showed columnar grains with a preferential orientation of  $\langle 001 \rangle$  converging at the center. The overlap zone between two adjacent contour lines had wider columnar grains with random orientations. Owing to different beam currents and scanning speeds in the hatch region than those in the contour region, the melt pool shape was expected to be wider and shallower in the hatch

region [78]. This melt pool geometry causes more grain growth from the bottom of the melt pool parallel to the building direction. In the overlap zone between two adjacent scan lines within one layer, grain nucleation and growth from the bottom of the previous melted scan line could occur. Deng et al. [78] reported that because of a higher overlap in the hatch than the contour region, more large bulk grains developed in the overlap zone in the contour region, while the grains were generally thin and elongated in the hatch region.

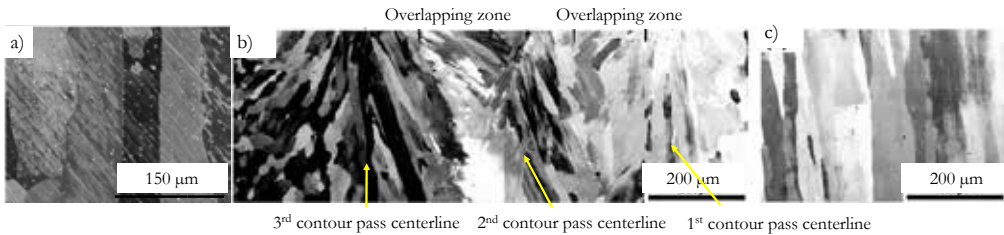


**Figure 2-10: SEM images of grain structure in; a) hatch region [76], b-c) contour and hatch regions [78].**

#### ***2.4.3.2 Melting strategies for grain structure tailoring***

Körner & Helmer et al. [57], [59], [79] applied local solidification conditions during EB-PBF by selecting specific machine-related parameters to tailor and control the grain structure. The columnar grain structures grew when the thermal gradient was parallel to the building direction. The equiaxed grains formed via a sharp change in the orientation of the thermal gradient from one layer to the other. By changing the direction of the thermal gradient from the build direction, the columnar grain growth was hampered, and the new nuclei started to grow. To tailor the grain structure using a linear melting strategy, a very low line offset, and very high scanning speed were applied. In this setting, individual melt pools were not distinguishable because of the very high overlap zone between the melt pools, and they were replaced by nearly flat lines indicating the individual layers. At the low line offset, the thermal gradient and its spatial variations at the solidification front became smaller, but the solidification direction changes increased. In this condition, the temperature gradients were shifted away from the building direction towards the traverse direction of each layer. One potential mechanism for grain nucleation was reported to be dendrite fragmentation, which could occur if the current solidification conditions and the underlying dendritic concentration profiles did not match. Because the orientation of the thermal gradient/solidification direction varied in every layer, the preferred growth direction also varied. The nuclei present at the bottom of the melt pools could, therefore, be better aligned to the thermal gradient than columnar grains, which were well aligned with the thermal gradient of the previous layer. Thus, the new nuclei could easily overgrow the columnar grains within one layer. This

## BACKGROUND AND MOTIVATION

mechanism repeated itself in every layer, leading to the formation of the fine grain structure. In this melting strategy, nucleation is mainly influenced by the change in the direction of the solidification/thermal gradient and not by the change in the magnitude of the thermal gradient and solidification rate. Thus, a change in the hatching direction results in the generation of different preferred growth directions of the current layer with respect to the previous one. Therefore, the grains solidifying in the previous layer can be mis-orientated with respect to the steepest temperature gradients in the next layer, leading to a higher tendency to form stray grains.

The influence of the beam spot size on the grain structure was also studied [57]. A more focused beam/smaller beam diameter increased the formation of new grains and prevented the development of the columnar grain structure, as shown in Figure 2-11. One potential reason for the formation of new grains with the focused beam was reported to be the more vigorous motion of the melt pools. The higher temperatures and higher temperature gradients in the melt pools due to the focused beam resulted in the fragmentation of dendrites and the formation of nuclei for the new grains. The other reason could be the stronger deviation of the solidification direction from the build direction and the changes in the dendrite arm orientation into a larger constitutionally undercooled volume where grain nucleation could occur. Moreover, the grain width was also low for a focused beam, indicating more new grain formation ahead of the solidification front. In contrast, a less focused beam led to a lower maximum temperature at the melt pool, which resulted in the formation of wide and shallow melt pools where the thermal gradient was low and aligned to the build direction. Owing to the lower temperature in the melt pools, less material was vaporized, and a smaller pressure was applied on the surface of the melt pools. Under this condition, the epitaxial growth of the grains was dominant, which suppressed the grain nucleation ahead of the nucleation front. It was shown that the average grain width increased from the bottom to the top of the build, which means that the grain width was a function of the built height. The change in the grain width was rationalized by the growth competition theory between the grains with different orientations. The grains with  $\langle 100 \rangle$  orientation, which is the easy growth direction in the FCC structure, grew faster, and the other grains with different orientations delayed behind the liquidus isotherm to find higher driving forces.

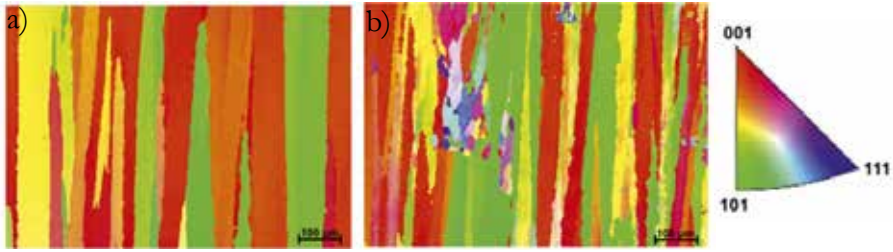


**Figure 2-11: EBSD orientation maps of the EB-PBF manufactured samples with a) defocused beam and b) focused beam [57].**

Regarding the tailoring of grain structures from columnar-to-equiaxed structures with random textures, Kirka, Dehoff, Cakmak, and Raghavan et al. [80]–[85] developed a point melting strategy in the hatch region. In this strategy, the main parameters were the beam current, the “beam spot on time”—which is the beam exposure time at one point, the spacing between adjacent points, and the number of point skip or point order number similar to line order number function described in Machine-related parameters. In the point melting strategy, the entire layer was filled with independent points. In this strategy, the adjacent melt pools were expected to be distinct, and their solidification was assumed to be independent of each other (see Figure 2-12). However, in the resulting microstructure, the adjacent melt pools were indistinguishable, which means that the individual melt pools did not solidify completely before the electron beam hit the next point. By increasing the energy input, the transition from the columnar to mixed grain structure (columnar with fine equiaxed), and finally, to a fully equiaxed grain structure, occurred. It was believed that by increasing the energy density, the initial melt pools became larger in size, and the heating frequency of the beam was fast enough to amalgamate the individual melt pools. Thus, all melt pools occurring in successive rows could merge into one another to turn the entire area molten. In low/medium energy input, there was not enough overlap of the melt pools, leading to a complete breakdown of the columnar structure, which resulted in a periodic columnar structure with a distance equal to the point skip spacing. The formation of more equiaxed grains was claimed to be affected by the turbulent fluid flow within the melt pools. The width of the obtained equiaxed grain structure was found to be approximately the one to two-layer thicknesses used in the build. The presence of coarser grains in the as-built part can be associated with the relatively slow cooling rate when compared to the grain sizes in the standard linear melting strategy. Through the applied melting strategy, the texture was also shown to change from the strong texture in the  $\langle 001 \rangle$  direction aligned parallel to the build direction to a random texture owing to temporal and spatial changes in the thermal gradient and growth rate.

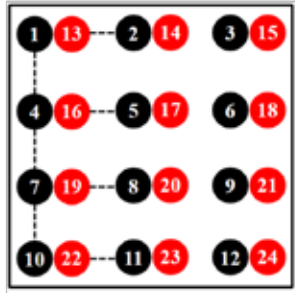


**Figure 2-12: Schematics illustrating point melting strategy. The point melting strategy consists of melting individual ‘points’, one point at a time in a pattern [85].**

#### ***2.4.3.3 Effect of focus offset***

The focus offset was shown by Im et al. [86] to be a critical parameter in controlling the solidification microstructure. The focus offset affects the shape of the melt pools, which directly impacts both the thermal gradient and the solidification rate. To obtain epitaxial growth, continuous melt pools must be formed, and the underlying layers must be sufficiently remelted. Discontinuous melt pools are unable to induce epitaxial growth owing to multi-directional heat flow as well as insufficient remelting. In contrast, the short and deep melt pools, which have pronounced curvature at their trailing edges, can produce columnar grains in the central longitudinal plane of the melt pool. Moreover, Lee et al. [75] showed that increasing the focus offset above a certain point causes the formation of broad and shallow melt pools. The lower energy input between the consecutive layers leads to the formation of more voids due to the presence of the unmelted powder particles. As a result, equiaxed grains and narrow columnar grains are formed around the voids at higher focus offsets.

#### ***2.4.3.4 Effect of part location***

The effect of the part location on grain size, morphology, and texture was studied by Kotzem et al. [50], who reported no significant differences in the size of the columnar grains. The length of the grains in the parts manufactured at different locations was above  $1500\ \mu\text{m}$ . The width of the grains in the interior regions on the build plate was  $131 \pm 8\ \mu\text{m}$ , while it was  $166 \pm 28\ \mu\text{m}$  in the exterior regions. All parts showed the same grain morphology and almost the same grain dimension and texture, which means that the differences in the thermal gradient were not sufficiently large to change these properties. Goel et al. [87] also reported similar findings regarding the grain structure and the change in the width of the grains at different locations on the build plate.

#### ***2.4.3.5 Effect of energy input, preheating, bed type (build plate, and powder)***

Ding et al. [74] studied the grain structure in single tracks. Columnar grains were observed in almost the entire cross-section of the single tracks, regardless of the process parameters. They reported that preheating increased the degree of nucleation near the bottom of the melt pools because of the lowered temperature gradient. The grain size in a single track was greatly affected by the size of the grains (width) in the bed material (either powder or build plate) because of the epitaxial growth. The grain size was significantly smaller when using a powder bed beneath the single tracks than when using a bulk bed with no powder. This was probably owing to the finer grain size in the powder, which resulted in the presence of more grain boundaries and more nucleation sites. A build plate with coarse grains leads to the formation of a coarse columnar structure in the single tracks.

In another study [88], the beam current levels and scanning speed were adaptively optimized using a new approach known as the adaptive offset method. In this approach, the line offset was altered based on the geometry of the melt pools of adjacent scanning lines. Fully columnar grains and a mixed columnar-equiaxed grain structure were observed. The mixed grain structure was formed under two different settings with extreme conditions. In the first setting, which had low line energy input and small line offset, the formation of the equiaxed grains was related to the presence of defects. In this setting, the columnar grains were found before the defects, whereas the equiaxed grains were found after the defects. However, in the second setting, in which high line energy input and large line offset were used, the equiaxed grains formed because of the deviation of the thermal gradient direction from the build direction owing to the formation of deeper melt pools.

The effect of spot energy density, which is the amount of heating in the build area, in the point melting strategy, on the formation of the equiaxed grain structure was evaluated by Knapp et al. [89]. A higher spot energy density increased the initial temperature of the powder bed, increased the time of solidification, and lowered the thermal gradient, which increased the probability of the equiaxed grain formation. One potential reason is the formation of a larger undercooled region. Additionally, a much longer solidification time means that there is a possibility for multiple spots to reach each other during melting, provide larger melt pools with a lower temperature gradient, and increase the probability of creating equiaxed grains.

In another work [84], the effects of beam current, beam diameter, beam-on time, and preheating temperature on the fraction of the equiaxed grain formation were evaluated. The volume fraction of the equiaxed grains increased with an increase in the beam diameter (least affecting parameter), beam current, beam-on time,

## BACKGROUND AND MOTIVATION

and preheat temperature (most affecting parameter) through a reduction in the temperature gradient.

### ***2.4.3.6 Effect of in situ heat treatment***

Sames et al. [72], [90], [91] reported that the variations in the thermal gradient, solidification rate, peak temperature, cooling rate, and the number of thermal gyrations/cycles are key factors in controlling the morphology of the grains and crystallographic texture. The microstructure evolution was controlled using *in situ* solution treatment and aging by heating the top surface of the part during the cooling process. Columnar grains with a length greater than 700  $\mu\text{m}$  were observed, which was much larger than the grain size found in the samples built using the Arcam recommended theme. Large grains were formed due to the longer holding time at an elevated temperature (approximately 1065  $^{\circ}\text{C}$ ). The grain growth mechanism was related to the  $\delta$  phase with a solvus temperature of approximately 1020  $^{\circ}\text{C}$ . During *in situ* solution treatment at a temperature above the solvus temperature of  $\delta$ , the grain boundary  $\delta$  phase is typically dissolved, which facilitates grain growth. However, the presence of  $\delta$  at the grain boundaries would not allow for grain growth during aging. Moreover, a part of the grain growth could have happened in the previous layers during the addition of the new layer owing to the high process temperature.

### **2.4.4 Common phases**

The microstructure of Alloy 718 is highly complex, with several phases in the  $\gamma$  matrix that modify the alloy properties based on their composition, morphology, and location. A summary of the common phases observed in EB-PBF manufactured Alloy 718, depending on the thermal profile of the process, is given in Table 2-1. The control and prediction of the phases in EB-PBF are highly complex. The formation of phases can be influenced by solidification and solid-state phase transformation, whereas subsequent melting/remelting and holding at elevated temperatures leads to significant changes in the characteristics of the present phases. The complex thermal histories present in EB-PBF have allowed researchers to rationalize the phase formations due to solid-state phase transformation, but more work is needed to predict microstructures. The very limited number of studies has not yet truly demonstrated the capability of process control to produce desirable phase structures via solidification or solid-state phase transformation.

**Table 2-1: Common phases observed in EB-PBF manufactured Alloy 718 [6], [63], [68]**

Phase	Crystal structure	Formula	Solvus temperature (°C)
$\gamma$	FCC	-	1260-1364
$\gamma'$	FCC	$\text{Ni}_3(\text{Al}, \text{Ti})$	850-910
$\gamma''$	BCT	$\text{Ni}_3\text{Nb}$	910-940
$\delta$	Orthorhombic	$\text{Ni}_3\text{Nb}$	1020
MC	Cubic	$\text{TiC}, \text{NbC}$	1260-1305
Laves	Hexagonal	$\text{Fe}_2\text{Nb}, \text{Fe}_2\text{Ti}, \text{Fe}_2\text{Mo}, \text{Fe}_2\text{Ta}, \text{Fe}_2\text{Ti}$	1163

- *$\gamma$  phase*: an austenitic solid solution phase that can maintain its structure up to its melting temperature. This phase has a high capacity for solid solution strengthening by elements such as iron, chromium, and molybdenum. These elements have 1–13% larger atomic diameters than nickel, and their strengthening effect is related to the atomic oversize [68].
- *$\gamma'$  phase*: an intermetallic strengthening phase that is coherent with the  $\gamma$  matrix. Typically, the morphology and size of  $\gamma'$  (from spherical to cuboidal) vary with temperature and exposure time. Apart from the thermodynamic effect, the chemical variations, such as the molybdenum content or aluminum/titanium ratio, can change the morphology of  $\gamma'$ . In general, by increasing the lattice mismatch between  $\gamma$  and  $\gamma'$ , the morphology changes in the following order: spherical, globular, blocky, and cuboidal. The aluminum/titanium ratio should be above 1.5 to promote the precipitation of stable  $\gamma'$  [63], [68], [70].
- *$\gamma''$  phase*: the main intermetallic strengthening phase, which is semi-coherent with the  $\gamma$  matrix. The  $\gamma''$  phase often forms together with the  $\gamma'$  phase in Alloy 718, and its precipitation is strongly dependent on the local niobium concentration. The  $\gamma''$  precipitates are usually disk-shaped. In Alloy 718, the lattice mismatch between  $\gamma''$  and  $\gamma$  (2.86 %) is greater than that between  $\gamma'$  and  $\gamma$  (<0.5 %) [92], [93]. Furthermore, the volume fraction of  $\gamma''$  ( $\gamma''/\gamma'$  is approximately 3.0 [93]) is higher. Therefore,  $\gamma''$  is the principal strengthening phase, whereas  $\gamma'$  contributes to the strength to some extent. One of the main drawbacks of the  $\gamma''$  phase in comparison to  $\gamma'$  is its transformation to the  $\delta$  phase at very high temperatures for very long exposure times [70].
- *$\delta$  phase*: the formation of different morphologies of the  $\delta$  phase is highly dependent on the time-temperature profile of the material [68]. The  $\delta$  phase is incoherent with the  $\gamma$  matrix. Because the precipitation of  $\delta$  occurs at the expense of niobium, which is associated with the loss of  $\gamma''$ , the formation of  $\delta$  is a potential reason for the reduction in strength. At low temperatures (650–700 °C),

## BACKGROUND AND MOTIVATION

the  $\delta$  phase can be observed at the grain boundaries [94]. By increasing the temperature to 750–800 °C, the transformation  $\gamma'' \rightarrow \delta + \gamma'$  occurs, which leads to the formation of  $\gamma''$ -free regions surrounding the particles of the  $\delta$  phase. The main reason for this transformation is the growth of the  $\delta$  phase, which results in the formation of dislocations, which may, in turn, produce more stacking faults in  $\gamma''$  and therefore promote  $\delta$  phase formation [94], [95]. An additional reason is the metastable nature of the  $\gamma''$  phase in Alloy 718, which can convert to the stable  $\delta$  phase with a plate-like morphology under thermal exposure [68]. Through a continuation of the aging process, the intragranular  $\delta$ -plates and/or  $\delta$ -plates formed from the  $\gamma''$  transformation may grow from the grain boundaries into the matrix. At 900 °C, the  $\gamma''$  phase is completely replaced by the  $\delta$  phase. The highest growth rate of the  $\delta$  phase has been observed at approximately 900 °C for the short-term aging of a material or a solutionized material [96]. The  $\delta$  phase presents some benefits with respect to the microstructure and mechanical properties in certain situations. The  $\delta$  phase frequently lies at the grain boundaries, which is the key to grain size control and to preventing notch sensitivity, which can be a major concern for the EB-PBF of Alloy 718 during the service life [90], [97].

- *Laves phase:* Depending on the thermal history of the material during the EB-PBF process, the Laves phase can form. The formation of the Laves phase was reported in relatively large parts, mainly at the top layers [32]. In fact, the segregation of elements, such as niobium and molybdenum, during solidification, creates interdendritic regions that are niobium-rich, which, if not properly homogenized, can form the Laves phase [6]. As a result of niobium segregation, the matrix is depleted of this element for the principal strengthening phase  $\gamma''$ ; therefore resulting in a reduction in the strength. The Laves phase is an intermetallic phase that is brittle in nature and detrimental to mechanical properties. The morphology of the Laves phase is typically in the form of irregular-shaped globules, which are often elongated, or platelets after extended high-temperature exposure [70], [98], [99].

- *MC-type carbides:* They are the most common carbide that forms in Alloy 718 during the EB-PBF process, with a predominantly globular/blocky morphology. Here, “M” is mainly niobium owing to its high content in Alloy 718; however, it can also be titanium or tantalum. As already discussed in the section on strengthening mechanisms, MC-type carbides can be beneficial or detrimental to mechanical properties depending on the size and the distribution region (intragranular or intergranular regions). Intragranular MC-type carbides have a lower strengthening effect (compared to the strengthening effect of the  $\gamma''$  phase) that is produced by hindering the movement of dislocations in the matrix of Alloy 718 [68], [100].

#### ***2.4.4.1 Phase evolution and influence of process parameters***

A summary of the present phases in the EB-PBF of Alloy 718, with their characteristics and formation mechanisms, is briefly presented. Moreover, the effects of some critical process parameters (which are under the scope of this research) on the present phases in the EB-PBF of Alloy 718 are explained.

Strondl et al. [76], [77], [101] reported the presence of carbo-nitride ((Nb,Ti)(C,N,B)) precipitates orientated in the same crystal directions as the FCC  $\gamma$  matrix. The carbo-nitride particles were aligned in rows along the build direction (at the interdendritic regions), and their sizes were in the range of 0.2–2  $\mu\text{m}$ . The distance between the rows was approximately 10–20  $\mu\text{m}$ . Some TiN precipitates were found in the as-built condition with a size below 5  $\mu\text{m}$  in diameter. It was reported that TiN particles form at all stages of solidification if the nitrogen concentration is above 40 ppm (40 ppm is the maximal solubility concentration of N in the  $\gamma$  phase at the liquidus temperature in Alloy 718). These particles also act as nucleation sites for carbide particles. Moreover, with a smaller amount of nitrogen, there will be a delay in carbide precipitation due to the lack of TiN nucleation sites. The  $\delta$  phase with a plate-like morphology, a length below 10  $\mu\text{m}$ , and a thickness of 100 nm were observed. The  $\delta$  phase precipitates also formed rows perpendicular to the layers, which most likely formed in the spacing between dendrites or cells because they are the last area to solidify. The  $\delta$ -phase formation was responsible for both the loss of niobium from the matrix and the  $\gamma''$  coarsening.  $\gamma'$  precipitates with sizes of 2–5 nm and  $\gamma''$  precipitates with sizes of 5–10 nm were also observed. Additionally, at small angle grain boundaries, coarser  $\gamma''$  precipitates 50–100 nm in size were observed. It was noted that the  $\gamma'$  and  $\gamma''$  precipitates were formed during cooling and the  $\gamma'$  precipitates were always found adjacent to the  $\gamma''$  precipitates.

Sames et al. [90] reported that phases in the as-built condition were affected by three specific stages of microstructural evolution: 1) rapid cooling from the melting temperature to the process temperature, 2) extended holding time at the process temperature, and 3) cooling to room temperature (below 100 °C). Based on this thermal history, a coarser  $\delta$  phase at the top and finer  $\delta$  phase at the bottom of the part were found, as shown in Figure 2-13. The  $\delta$  phase was present within the matrix and at the grain boundaries, at which the  $\delta$  phase usually forms first. The  $\gamma'$  precipitates had a cuboidal morphology with an average size of 60 nm. The  $\gamma''$  phase appeared in two different sizes, i.e., 65 nm with a rod shape and 35 nm with a disc shape morphology on the surface of  $\gamma'$ . Both the  $\gamma'$  and  $\gamma''$  precipitates were present within the  $\gamma$  matrix near the  $\delta$  phase. In general, the precipitation of the intragranular  $\delta$  phase takes place when metastable  $\gamma''$  precipitates transform to the stable  $\delta$  phase, which is expected at a high temperature. During the melting process, the bottom layers of the samples were held at a high temperature near or just above the substrate temperatures for an

## BACKGROUND AND MOTIVATION

extended time. At the top layers, the average temperature is expected to be 1000 °C, which is higher than the holding temperature of approximately 970 °C at the bottom layers, which induced the coarser  $\delta$  phase at the top of the build.

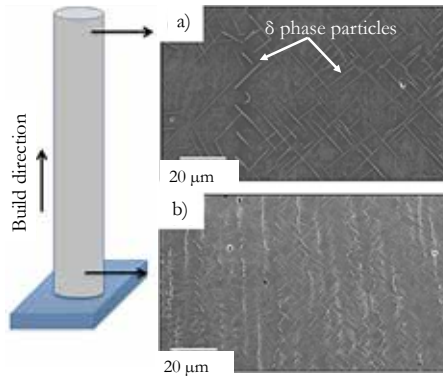


**Figure 2-13: SEM images parallel to the build direction from; a) the top, and b) the bottom of the sample [90].**

The phases in three different conditions—i) *in situ* heat treatment after the build was finished, ii) fast cooling rate, and iii) slow cooling rate—were also compared [91]. The *in situ* heat-treated part did not form large quantities of the intragranular and needle  $\delta$  phases. This might be because the long holding time for the *in situ* heat treatment was not in the temperature range needed for the direct precipitation of the  $\delta$  phase from the matrix, while the holding temperature for the *in situ* heat treatment was within the range for the formation and coarsening of  $\gamma''$  and  $\gamma'$ . Further analysis showed that a decrease in the final cooling rate resulted in the formation of large and elongated  $\gamma''$  disks. In both cases of slow cooling rate and *in situ* heat treatment, uniformly distributed  $\gamma''$  and  $\gamma'$  were observed at the grain interiors.

Kirka et al. [32], [102] similarly reported a gradient in the observed phases in a material, which was classified into three distinct regions. Region 1, which was the top of the build (the top 8 to 10 layers), included the carbides and Laves phase within the interdendritic regions. The average size of the  $\gamma''$  precipitates was 80 nm, which was assumed to precipitate after the completion of the build. The presence of  $\gamma''$  in the final layer could be due to the temperature-sensitive  $\gamma''$  precipitation kinetics requiring a minimum holding time of 600 s for precipitation at 850 °C under the most optimal conditions. In Region 2, which was further down, the Laves phase was replaced by small networks of  $\delta$  needles (500 nm in length) in the interdendritic regions. The grain boundary  $\delta$  phase was found in this region, which could most likely be associated with the presence of niobium sourced from the dissolution of the Laves phase. Region 3 contained networks of

the intragranular  $\delta$  phase. With the precipitation of the intragranular  $\delta$  phase in this region, the surrounding matrix became denuded of  $\gamma''$ , which resulted in the reduction in the size of  $\gamma''$  to 35 nm at the bottom of the build. The observed transition of the microstructure was attributed to the short diffusion distances in such a fine-scale microstructure and significant building time.

Deng et al. [78], [103] also characterized the phases in the as-built conditions and reported that carbides were more likely to precipitate in the interdendritic regions. The carbides with a blocky shape were smaller than  $2\ \mu\text{m}$  and were found to be distributed either intragranularly or intergranularly. The carbides were typically nucleated on the TiN or  $\text{Al}_2\text{O}_3$  particles. The  $\text{Al}_2\text{O}_3$  might be directly inherited from the powder feedstock, or it can be formed during processing through a reaction between the aluminum and residual oxygen in the build chamber. Very fine plate-like  $\delta$  precipitates with a size of approximately 100 nm were detected only at the high-angle grain boundaries because of the easy diffusion of niobium along these boundaries. During the process, the build plate temperature was kept constant at approximately  $1000\ \text{°C}$ , which was assumed to be above the solvus temperature of the  $\delta$  phase. Thus, the  $\delta$  phase was not expected to precipitate during the building process. However, during the cooling step, when the build was finished, the thermal profile could possibly fall in the  $\delta$  phase temperature precipitation zone. Therefore, the  $\delta$  phase can directly precipitate from the supersaturated  $\gamma$  matrix. Only a few  $\delta$ -phase particles were found at the bottom of the part, which might be due to very rapid cooling at the bottom regions. The heat sink through the build plate limited the precipitation of the  $\delta$  phase.

A gradient in the volume fraction of the Laves phase at the top region of the part was reported [103]. The amount and size of the Laves phase are greatly affected by the cooling rate and the holding time in the building temperature, which causes *in situ* homogenization. At a certain distance from the top of the build ( $1800\ \mu\text{m}$ ), there was no microstructural gradient. The volume fraction of the Laves phase increased from zero at the top surface to approximately 2.3% at  $150\ \mu\text{m}$  from the top surface, which then gradually decreased to approximately zero again at  $1800\ \mu\text{m}$  from the top surface. A similar trend was reported for the size of the Laves phase. This trend was related to the temperature, which was high enough to gradually dissolve the Laves phase and homogenize the distribution of niobium during the building process. The size of the Laves phase was more than  $10\ \mu\text{m}$  in length and approximately  $2\text{--}3\ \mu\text{m}$  in width at the top regions, whereas the phase became smaller at the bottom regions. Considering the relatively slow dissolution kinetics of the Laves phase and poor diffusivity of niobium, the thermal condition was still sufficiently high to dissolve the remaining Laves phases. The carbide/nitride/carbo-nitride was barely affected by *in situ* homogenization during the process, and their presence in the partly- and fully homogenized regions was not height-dependent. These particles stayed in their as-solidified

## BACKGROUND AND MOTIVATION

condition due to their high stability. The average volume fraction of the particles remained similar throughout the partly and fully homogenized regions.

In contrast to Sames and Deng et al., Sun et al. [104] reported a greater amount of the  $\delta$  phase in the bottom layers of the part than in the top layers. They believed that this could be due to the *in situ* aging/longer holding time at elevated temperatures for the bottom layers during the process, which extends until the completion of the built part. They also reported that the thickness and length of the  $\gamma''$  precipitate were approximately 4 nm and 16 nm, respectively, in the as-built conditions.

- *Effect of focus offset and energy input*

The effect of the focus offset on the  $\gamma''$  size was examined by Im et al. [86]. The average  $\gamma''$  size became larger with an increase in the focus offset in a specific range. A higher focus offset yielded a longer exposure time at the temperature range of the  $\gamma''$  precipitation. The longer exposure time resulted in a slower cooling rate and more repeated thermal cycles due to the greater overlap zone.

Lee et al. [75] reported that the thickness of the Laves phase increased with the focus offset, while the size of the carbides did not change. The Laves phase and  $\delta$  precipitate were mainly formed intergranularly, while the carbides were developed intra- and inter-granularly. The increased focus offset led to a lower cooling rate and longer holding time in the temperature range of the  $\delta/\gamma''$  and  $\delta/\gamma'$  phase transformations. Therefore, the parts built with high focus offsets had higher volume fractions of the  $\gamma'$  and  $\gamma''$  precipitates. Moreover, the size of the  $\gamma''$  precipitates was found to be in the range of 2.52–5.03 nm with an increased focus offset owing to the longer holding time at the transformation temperature range. 3D reconstructed  $\gamma'/\gamma''/\gamma'$ , and  $\gamma'/\gamma''/\gamma'/\gamma''/\gamma'$  sandwich structures were found on the  $\gamma$  matrix, which was parallel to the build direction and was very thin to interrupt the movement of the dislocations. The  $\gamma''$  precipitates preferentially nucleated during the aging treatment, and niobium was depleted from the  $\gamma$  matrix adjacent to the  $\gamma''$  precipitates. There was a local enrichment in the levels of manganese and aluminum, and the oversaturated region close to the surface of the  $\gamma''$  precipitate became a preferential nucleation site for the  $\gamma'$  precipitates. As a result,  $\gamma'$  precipitates were formed on both sides of the  $\gamma''$  precipitates to form the  $\gamma'/\gamma''/\gamma'$  sandwich.

Ding et al. [88] conducted a study on energy input effects by changing the beam current, scanning speed, and line offset of the phases and observed that the sizes of the carbides were approximately several hundred nanometers, while the  $\gamma'$  and  $\gamma''$  phases were smaller than 30 nm. The size and morphology of precipitates in the parts built with different parameters were almost the same. The  $\gamma''$  phase had

an average thickness of approximately 10 nm and a length of approximately 30 nm, and the  $\gamma$  phase had an average size of approximately 20 nm.

## 2.4.5 Internal and external defects

Defects, including internal and external defects, are detrimental to the mechanical properties as they facilitate crack initiation and propagation [6], [34], [105]. The internal defects are linked to the bulk, which includes round pores, shrinkage pores, lack-of-fusion (LoF), and cracks. The external defects are related to the surface of the part, which includes surface cracks and balls/satellites attached to the surfaces. In this section, the effects of some critical position- and machine-related parameters on the formation and portion of the defects are briefly discussed.

### 2.4.5.1 Internal defects

**Round pores** are mainly sourced from feedstock materials (e.g., feedstock powder). The origin of the round pores in the powder particles is the gas (usually an inert gas such as argon) trapped inside the particles during the powder manufacturing process [106], [107]. The round pores can transfer directly to the as-built parts. In the EB-PBF process, owing to the rapid solidification of the material, the trapped gas within the gas- or plasma-atomized powders has insufficient time to escape from the melt pool, even though the vacuum level is high; see Figure 2-14a [6].

**LoF** is a major defect in EB-PBF and is mainly dominated by machine-related parameters. This implies that the machine-related parameters must be properly set/optimized to reduce the formation of LoF defects. The size of the LoF defects can range from a few micrometers to a few millimeters, and the morphology is mainly irregular. A potential reason for the formation of LoF defects is a lack of sufficient applied energy input to completely melt the particles, as some unmelted powder particles can be seen within these pores. Alternatively, a high applied energy density can cause the spattering of the melted material away from the melt pool, leading to the formation of LoF defects (see Figure 2-14b) [6], [27], [49].

**Shrinkage pores** are a collection of round-shaped pores that form a band at certain regions, mainly in the interdendritic regions along the build direction [77]. The dominant mechanism that induces shrinkage pores is the residual thermal stress generated during solidification. Shrinkage defects occur because of the volume reduction of the melted material during cooling and solidifying. Generally, during the solidification of the top molten layers, the material shrinks, and its volume decreases. This shrinkage is hindered by underlying layers that have been previously processed [108]; see Figure 2-14c.

## BACKGROUND AND MOTIVATION

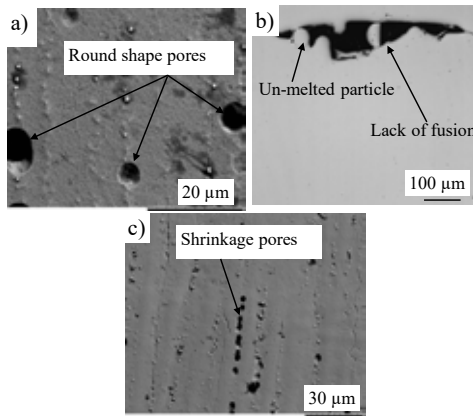


**Figure 2-14: SEM and LOM images of a few defects observed in EB-PBF of Alloy 718.**

Deng et al. [78] reported that the overall defects in the as-built part in the contour and hatch regions were approximately 0.6 % and 0.2 %, respectively. LoF defects were also observed at the contour/hatch interface, which was attributed to the lower melt pool stability at the interface. Shrinkage defects with a size of less than 2 μm appeared to be aligned along the grain growth directions and formed strings when viewed parallel to the build direction. However, round pores were not observed because of the use of a pore-free feedstock powder.

**Cracking** may occur during solidification or subsequent cyclic heating. Solidification cracking is common in the EB-PBF of Alloy 718, which is dependent on the alloy composition, solidification mode of the solidified material (dendritic, cellular, or planar), and energy input. Solidification cracking can be formed by high strain and stresses on the melt pools, poor flow of liquid, or flow obstruction by the solidified grains. If too much energy input is used, a higher thermal gradient forms, which can cause the larger thermal stress required for solidification cracking [72]. This type of crack can be observed along the grain boundaries due to the formation or dissolution of the precipitates, and along the grain boundary angles [109], [110] (see Figure 2-15). Another type of crack is strain age cracking, which generally occurs in the solid-state post thermal treatment or subsequent cyclic heating in the EB-PBF process. In fact, if the residual stresses resulting from the building process exceed the fracture stress at some location in the material, then strain age cracking is more likely to occur. Sames et al. [91] noted that an abnormal high-temperature during melting might allow hot tearing or liquation of the interdendritic solidification phases to form cracks. They reported significant cracks in the parts, aligned parallel to the columnar grains, and the build direction. The length of the cracks was reported to be greater than 850 μm. The cracks did not lay at the grain boundaries all the

time, but the cracking tendency was liquated near the carbide regions. The cracks had some serrated edges, which could be related to cracking during a semi-liquid solidification state. This form of cracking was shown to be associated with higher energy input.

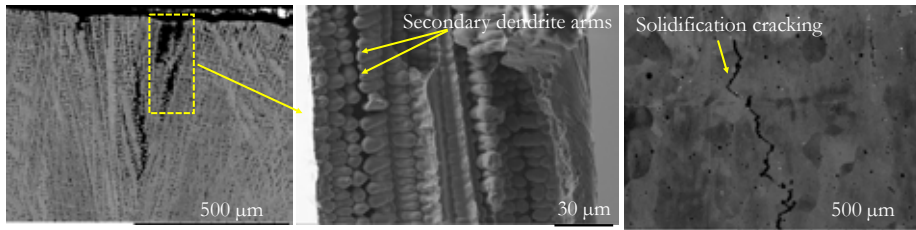


**Figure 2-15: SEM images of solidification cracks observed in EB-PBF of Alloy 718.**

Regarding the residual stress, Prabhakar et al. [111] reported that the origin of residual stress is either i) differential heating of the solid, which forms large thermal gradients or ii) differential cooling. The maximum temperature applied to each layer of the build was assumed to be 1500 °C, and the build plate was at an initial temperature of 1000 °C. It was observed that the influence of temperature applied on the layers was reduced by the addition of layers. This implies that the thermal impact was restricted to a few top layers of the build with a reduced influence on the build plate. Thus, stresses and plastic strain accumulation in the build plate appeared to be high towards the end of the process. Four recommendations were made to lower the level of residual stresses in the build plate as follows: 1) increasing the thickness of the build plate, 2) choosing a build plate made of the same material as the build material, 3) increasing the temperature of the build plate and powder bed during the initial sintering steps prior to layer melting, and 4) choosing a gradual cool down rate at the beginning followed by an exponential decay.

- *Effect of energy input, focus offset, geometry, and location*

The focus offset was recognized to play a major role in the relative density of as-built parts, as reported by Im et al. [86]. It was shown that lower focus offset values provided higher relative densities (above 99.9%). The relative density in the studied process window did not change sensitively with the beam current and scanning speed. Lee et al. [75] also investigated the influence of the focus offset on the density of the part and found that a low focus offset showed many microvoids with a very fine size of 10 μm. Larger macro-voids of approximately 200 μm and unmelted powders were exhibited at higher focus offset, which means that a high focus offset causes a large spot area with insufficient energy input. The

## BACKGROUND AND MOTIVATION

voids observed near the surface were mainly LoF defects with a size of 50  $\mu\text{m}$ . The reason for the formation of the LoF defects at a distance of 2 mm from the side surface was the difference between the process parameters in the contour and hatch regions.

Helmer et al. [57] found that the occurrence of defects such as LoF was due to insufficient energy input, causing shallow and small melt pools. Thus, one approach to reducing the defects was to increase the energy input by enhancing the beam current/reducing scanning speed to increase the melt pool volume. A reduction in the line offset to increase the overlap was suggested as an alternative solution. Ding et al. [88] also reported a low line energy input, and a small line offset caused substantial internal defects. By increasing the scanning speed, the critical line energy input required for building dense parts decreased, which led to the formation of shallow melt pools. At higher scanning speeds, less time was required to scan the same length, and less heat was lost by dissipation, which could contribute to the melt pool formation in the subsequent scan lines. Moreover, when the line energy input was not sufficient to form a melt pool deeper than the layer thickness, no connection could be made between the adjacent layers. As the line energy increased, the melt pool depth increased, and when it became larger than the layer thickness, the powder layer and previously solidified layer were melted together, forming a stable melt pool. However, in the extremely low line energy, a stable melt pool could not be formed owing to the balling phenomena in such a situation, which resulted in the formation of cavities in the final parts. Thus, round pores (with different sizes: small, joined, and large) tend to form when the energy input is too low. The small pore sizes were in the range of 1–2  $\mu\text{m}$ , and they were distributed all over the part. Some of the round pores were attached together with a similar width to the small pores; however, their lengths were up to 10  $\mu\text{m}$  parallel to the build direction. It was found that the small pores and joined pores were most likely caused by gas trapped in the powder, which was not released from the melt pool during the process. The large round pores had a diameter of 10–50  $\mu\text{m}$ . Because of the rough inner surfaces of the large pores, it is likely that they resulted from the raking process. The molten jets from the melt pool solidified on the top surface of the material and formed around particles that were attached to the surface. During the next raking process, this particle was removed by the raking blade, leaving a pit on the surface, which resulted in large pores. It was found that the small pores accounted for a higher proportion of the total porosity than the other two sizes.

The effect of geometry on the content of defects was examined by Sames et al. [72]. It was reported that a small specimen would reach a higher peak temperature during melting than a large specimen, given the same beam current and scanning speed, which could cause more LoF defects. This could be due to the lower

thermal conductivity of the powder in the small specimen. When heat is applied, it is conducted to the build plate more slowly through the powder, which can cause overheating of the melt surface located above the powder.

Kotzem et al. [50] showed that the location of the part on the build plate had a slight effect on the relative density. The maximum and minimum relative densities were reported to be 99.89% and 99.27% for the parts located in the center and exterior regions on the build plate, respectively. The relative density of the parts built on the right side of the build plate seems to be less than that on the opposite side. However, this deviation did not follow a clear and significant trend. In a similar study by Goel et al. [87], the defect content was found to be close to uniform along with the build height (negligible differences at the top and bottom of the part). At different locations (slight differences) on the build plate, the total defect concentration was below 1%.

#### ***2.4.5.2 External defects***

Surface-related defects are dependent on the machine-related parameters in the contour regions. In the EB-PBF process, the contours are typically built before the melting of the hatch region. The contour built after the melting of the hatch region tends to form more satellites owing to its higher temperature, yielding a rougher surface finish [72]. According to Im et al. [86], the focus offset is identified as a key parameter that determines the surface quality of the as-built parts. The surface roughness increased significantly (two times higher) when the focus offset was very high.

Kotzem et al. [50] reported a high geometrical deviation based on a comparison between the size of the manufactured part and the initial CAD data. The size deviation was up to 23%. The differences between the CAD data and the average equivalent diameter were significant in all the parts located in different positions on the build plate. Moreover, deviations marginally increased from the inside to the outside of the build plate. The average surface roughness values ( $R_a$ ) were found to be in the range of  $28.5 \pm 0.1$  to  $55.1 \pm 0.4 \mu\text{m}$ . Two types of surface defects were found, that is, plate-pile stacking features similar to stacking defects, and partially melted powder particles remained on the surface of the part. The plate-pile stacking features might be formed owing to the slightly varying melt pool shapes for every single layer, which is induced by the scanning strategy and melt pool dynamics.

#### **2.4.6 Hardness**

Strondl et al. [77] did not find a significant difference in the macro- and microhardness of the layers parallel or perpendicular to the build direction. In addition, no difference in hardness was observed between the bottom and top of the as-built parts. Goel et al. [87] also confirmed the same trend, indicating

## BACKGROUND AND MOTIVATION

uniform hardness along the build height and at different locations on the build plate. However, Kotzem et al. [50] reported that the hardness increased slightly from the inside to the outside of the build plate; however, no tendency between the right and left sides of the build plate was detected. The increased hardness in the outer locations on the build plate was reported to be due to a higher fraction of the strengthening phases. The average hardness values were in the range of 350–377 HV. Lee et al. [75] did not observe a significant difference in the microhardness between the top and bottom layers of the part. It was found that microhardness is predominantly affected by the focus offset, indicating that the volume fractions of the  $\gamma'$  and  $\gamma''$  precipitates depend on the focus offset.



## 3 Materials and experimental setup

The goal of this study was to gain a better understanding of the evolution and tailoring of the microstructural characteristics of Alloy 718 during the EB-PBF process. The influence of geometry-, position-, and machine-related parameters on the microstructural characteristics was investigated. Fine-scale and cubic samples were built using the EB-PBF process. All the techniques used to investigate the feedstock powder and the manufactured parts are briefly described in this chapter.

### 3.1 Feedstock powder

Both plasma-atomized (PA) and gas-atomized (GA) Alloy 718 powders were used. The PA powder was supplied by Arcam-EBM AB (Mölnlycke, Sweden), whereas the GA powder was supplied by Sandvik AB (Sweden). The chemical composition of the Alloy 718 powders provided by the suppliers is given in Table 3-1. The two powders were always used individually (which will be discussed later); however, a mixture of virgin and re-used powders was used to manufacture the parts.

**Table 3-1: Chemical composition of the PA & GA Alloy 718 powder provided by the suppliers (all in wt%)**

Element*	Ni	Co	Cr	Mo	Ti	Mn	Nb	P	Al	Si
Arcam-EBM	54.1	0.04	19	2.99	1.02	0.12	4.97	0.004	0.52	0.06
Sandvik AB	53.3	0.01	18.7	3.0	0.94	0.07	5.14	0.003	0.42	0.05

\* Fe was in Bal., S was below 0.001, C was approximately 0.03, and Ta was below 0.01 wt% in both powders.

The virgin PA powder had a spherical morphology; however, the GA powder had a mixture of irregular and spherical morphologies. Small satellite particles were attached to the surfaces of both powders (Figure 3-1a–d). After recycling the powders, agglomerated powder particles were found (Figure 3-1b). The content of the internal pores in the PA powder was low, and only small internal pores were observed in the cross-section of the powder particles; however, in the GA powder, the content of the internal pores was higher due to the manufacturing

process. The size distribution of the virgin powder particles in both GA and PA was approximately 45–105  $\mu\text{m}$  (diameter). Scanning electron microscopy (SEM) images of the cross-sections of the re-used PA powder particles showed some particles containing a fine secondary phase (Figure 3-1f). Energy dispersive spectroscopy (EDS) revealed that the secondary phase was rich in niobium, as shown in Figure 3-1, and was most likely a mixture of the  $\delta$  phase and niobium-rich carbides.

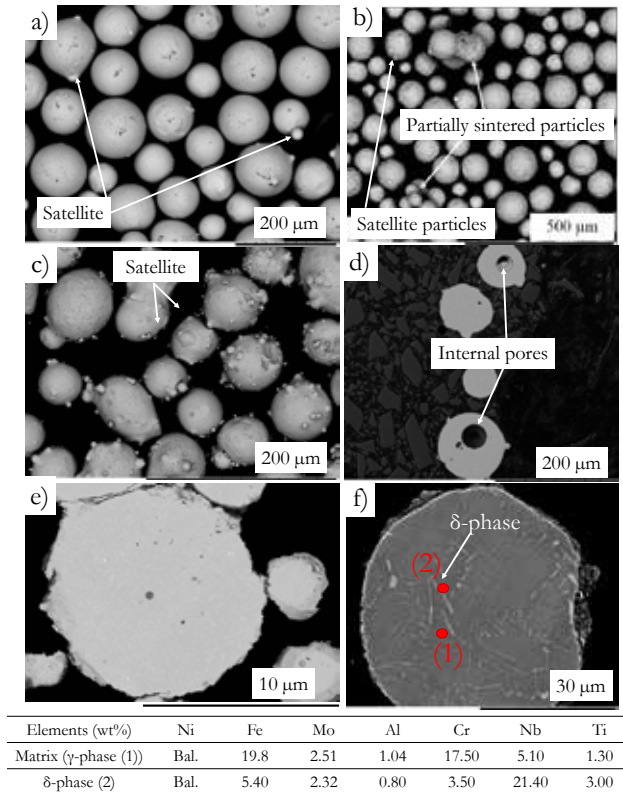


**Figure 3-1: SEM (BSE mode) images of the morphology and the cross section of the powder particles: a) virgin PA powder, b) re-used PA powder, c) virgin GA powder, d) virgin GA powder, e) virgin PA powder, and f) re-used PA powder.**

### 3.2 Sample manufacturing setup

The samples were manufactured using an Arcam-EBM machine (A2X, Mölnlycke, Sweden). The key machine-related parameters are briefly presented in

## MATERIALS AND EXPERIMENTAL SETUP

Table 3-2. More details of the sample manufacturing and design in each appended paper are presented as follows.

**Table 3-2: the key machine-related parameters for the EB-PBF manufactured Alloy 718 samples used in different papers appended to this thesis work**

Machine-related parameters	Paper A (Hatch)	Paper B (Hatch)	Paper C (Hatch)	Paper D (Hatch)	Paper E (Hatch)	Paper F (Contour)	Paper G (Hatch)	Paper H (Hatch)
Powder	Re-used	Re-used	Re-used	Re-used	Virgin	Re-used	Re-used	Re-used
Speed function	Off	Off	On	On	Off	Off	On	On
Layer thickness ( $\mu\text{m}$ )	75	75	75	75	75	75	75	75
Beam current (mA)	7	7	7	7	7-15	10-15	20, 25	10-15
Focus offset (mA)	15	15	15	15	0-10	10-20	15	15
Line offset ( $\mu\text{m}$ )	125	125	125	125	-	100, 300*	10	300-500
Scanning speed (mm/s)	1250	1250	1250	1250	300-1000	200-400	15000	400-800
Voltage (kV)	60	60	60	60	60	60	60	60
Scanning strategy	Uni- direction	Uni- direction	Bi- direction	Bi- direction	-	-	Uni- direction	Bi- direction
Hatch rotation	-	-	$67^\circ$	$67^\circ$	-	$67^\circ$	$90^\circ$	$90^\circ$

\* 100  $\mu\text{m}$  is the line offset between inner contour, and hatch region and 300  $\mu\text{m}$  is the line offset between the inner and outer contours.

In papers A and B, different geometry-related parameters were used to understand the microstructural evolution during the EB-PBF process. Both track (T)-by-track and layer (L)-by-layer (single wall) samples were manufactured using the Arcam recommended theme parameters for the hatch region of cubic samples of size  $20 \times 20 \times 20 \text{ mm}^3$ . All the samples were produced on an additional substrate, known as a stand, made of Alloy 718 using the Arcam recommended parameters (see Figure 3-2).

The track-by-track samples started from a single track and comprised up to 10 tracks that were next to each other, for example, TxL1 (x: 1, 2, 3, ..., 10). The layer-by-layer samples started from one and consisted of up to 50 layers (T1L1, T1L2, ... etc.). The length of the tracks was kept constant at 20 mm. Moreover, samples with five tracks and different numbers of layers were also produced to determine the effect of wall thickness.

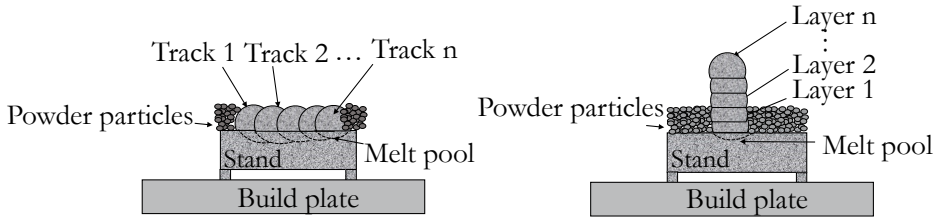


**Figure 3-2: Schematic of the track-by-track and layer-by-layer samples in papers A and B.**

In paper C, cubic samples in different groups (A, B, C, D, E, and F) were built on the build plate at a 45° angle; see Figure 3-3. The machine-related parameters recommended by Arcam were used to investigate the effect of the position-related parameters, such as the distance between samples, the height from the build plate, and the location of the sample on the build plate (see Figure 3-3).

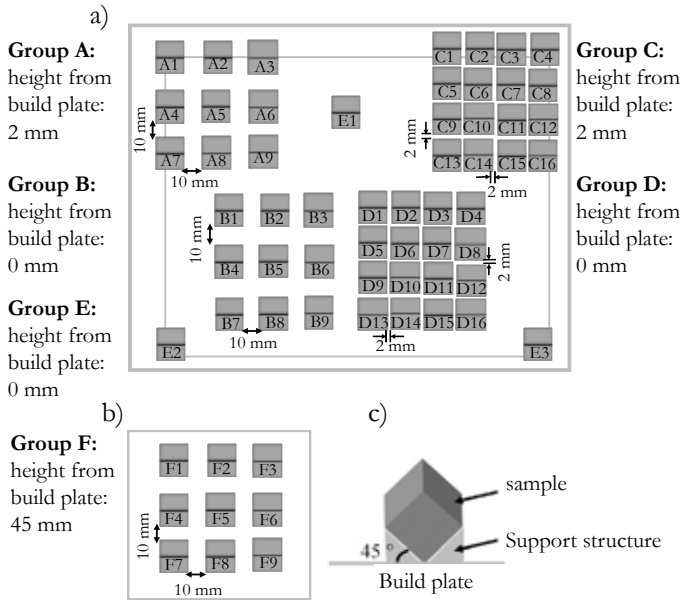


**Figure 3-3: Schematic of the top view of the position-related parameters in paper C: a) groups A, B, C, D, and E, b) group F, and c) orientation of the sample on the build plate.**

Owing to the limited number of samples for group E in paper C and no clear trend in the results for the effect of location on the microstructure, another set of cubic samples was built to reveal this effect, and the results were reported in paper D (Figure 3-4). Similar to paper C, the Arcam recommended theme was used to

## MATERIALS AND EXPERIMENTAL SETUP

manufacture the new batch of samples (four groups, including A, B, C, and D) in paper D to verify the repeatability of the previous results.

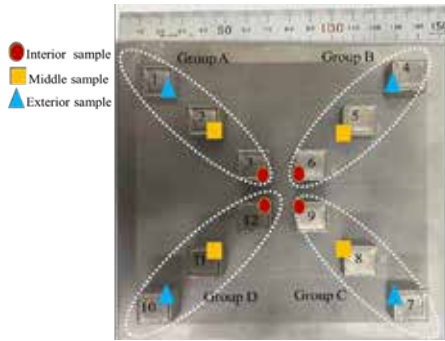


**Figure 3-4: Top view of the manufactured samples in four groups (A, B, C, and D) with different locations on the build plate in paper D.**

In paper E, the aim was to evaluate the effect of some critical machine-related parameters on the geometrical features, including track height ( $d1$ ), melt pool depth ( $d2$ ), melt pool width ( $w$ ), and contact angle average ( $\theta = (\theta_1 + \theta_2)/2$ )—see Figure 3-5—as well as the microstructural features of the single-track samples. A design of experiments (DoE) approach was implemented over a specific range for three machine-related parameters, including scanning speed, beam current, and focus offset, to determine the appropriate process window (see Table 3-3). In this design, a full factorial screening scheme across three levels was used. Each machine-related parameter set was repeated four times, and for each sample, two cross-sections were evaluated in order to increase the statistical significance of the experiment; see Figure 3-5.

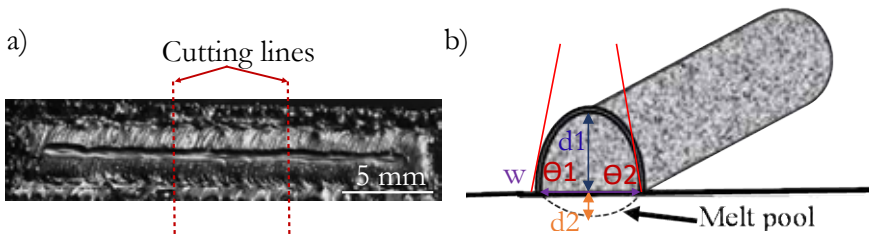


**Figure 3-5: a) Light optical microscopy (LOM) image of the top of a representative sample (# 7), and b) a schematic of the cross-section of a single track with its geometrical features presented in paper E.**

**Table 3-3: The machine-related parameter settings used in the full factorial three-level DoE screening in paper E**

<b>Trial #</b>	<b>Scanning Speed (mm/s)</b>	<b>Beam current (mA)</b>	<b>Focus offset (mA)</b>	<b>Linear energy input= Power/Scanning speed (J/mm)</b>
1	300	15	0	3.00
2	300	15	5	3.00
3	300	15	10	3.00
4	300	11	0	2.20
5	300	11	5	2.20
6	300	11	10	2.20
7	300	7	0	1.40
8	300	7	5	1.40
9	300	7	10	1.40
10	650	15	0	1.38
11	650	15	5	1.38
12	650	15	10	1.38
13	650	11	0	1.02
14	650	11	5	1.02
15	650	11	10	1.02
16	1000	15	0	0.90
17	1000	15	5	0.90
18	1000	15	10	0.90
19	1000	11	0	0.66
20	1000	11	5	0.66
21	1000	11	10	0.66
22	650	7	0	0.64
23	650	7	5	0.64
24	650	7	10	0.64
25	1000	7	0	0.42
26	1000	7	5	0.42
27	1000	7	10	0.42

In paper F, the results from the single-track studies were used to improve the surface quality and defects observed in the contour region and at the contour/hatch interface. In this work, the linear melting strategy was used in both the inner and outer contour regions, and a full factorial design of the experiment at two levels was applied to screen the three main machine-related parameters. It

## MATERIALS AND EXPERIMENTAL SETUP

must be noted that the line offset between the two contours and the offset between the contour and hatch were kept constant at 300  $\mu\text{m}$  and 100  $\mu\text{m}$ , respectively. In addition, one extra sample using the Arcam recommended theme for the contour region was also built with spot melting to compare with the linear melting strategy used in this study.

**Table 3-4: The machine-related parameter settings used for the full factorial two-level DoE screening in the contour region in paper F**

Trial #	Scanning speed (mm/s)	Beam current (mA)	Focus offset (mA)	No. of contours
1	200	10	10	1
2	400	10	10	1
3	200	15	10	1
4	400	15	10	1
5	200	10	20	1
6	400	10	20	1
7	200	15	20	1
8	400	15	20	1
9	300	13	15	1
10	300	13	15	1
11	300	13	15	1
12	200	10	10	2
13	400	10	10	2
14	200	15	10	2
15	400	15	10	2
16	200	10	20	2
17	400	10	20	2
18	200	15	20	2
19	400	15	20	2
20	300	13	15	2
21	300	13	15	2
22	300	13	15	2
23	Arcam recommended theme-spot melting with three contours			

The final goal presented in papers G and H was to develop proper melting strategies using different machine-related parameters to tailor the grain structures.

For this purpose, two different approaches were proposed. The first approach presented in paper G uses a tight line offset value ( $10\ \mu\text{m}$ ), different line order numbers (1, 5, and 10), two different beam currents (20 and 25 mA), and a very high scanning speed. In this design, if the line order number is one, melting is similar to the snaking (raster) melting used in the Arcam recommended theme, but in a unidirectional path. If the line order number is above one—for instance, 10—after melting the first scan line, the beam jumps to and melts the eleventh line. All lines with a 10-line intermediate spacing are melted. The beam then sequentially melts the 2<sup>nd</sup>, 12<sup>th</sup>, 22<sup>nd</sup> lines, and so on. This approach continues until the entire layer is melted (see Figure 3-6).

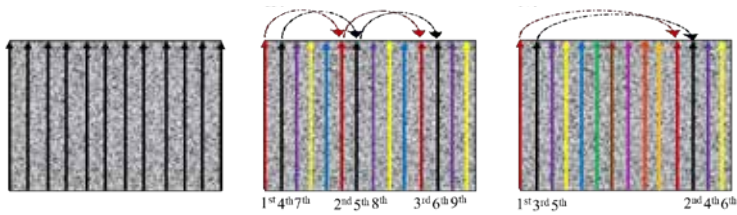


**Figure 3-6: Schematic of the proposed scanning strategy in paper G; a) line order number of 1, b) line order number of 5, and c) line order number of 10.**

Because of the promising effect of a higher line order number in facilitating the CET, in the second approach presented in paper H, the line order number was kept constant at 10. In the second approach, double melting was used for every single layer, meaning that each layer was melted twice; however, no powder was spread during the second melting (see Figure 3-7). The samples were manufactured based on a full factorial screening DoE at two levels for each parameter (see Table 3-5). Moreover, a wider range of the line offset from 300 to 500  $\mu\text{m}$  was used compared to the Arcam recommended value (125  $\mu\text{m}$ ).

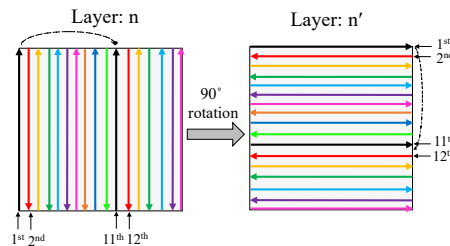


**Figure 3-7: Schematic of the proposed scanning strategy in paper H; a) line order number of 10 with double melting of each layer.**

**Table 3-5: The machine-related parameter settings used for the full factorial two-level DoE screening in paper H**

Sample #	Scanning speed (mm/s)	Beam current (mA)	Line offset ( $\mu\text{m}$ )	Energy per area (J/mm <sup>2</sup> )
1	400	10	300	5.0
2	800	10	300	2.5
3	400	10	500	3.0
4	800	10	500	1.5
5	400	15	300	7.5
6	800	15	300	3.75
7	400	15	500	4.5
8	800	15	500	2.2
9	600	12.5	400	3.1

### 3.3 Metallographic preparation

For characterization by light optical microscopes (LOM) and SEM, the fine-scale samples of track-by-track, layer-by-layer/single walls, and single tracks from the DoE were cut at two different points that were approximately 7 mm from the start and end points (see Figure 3-5a). The cubic samples were cut from the middle using an abrasive precision cutter for similar characterizations. All the samples were then hot-mounted in a non-conductive Bakelite holder. An example of a mounted sample is shown in Figure 3-8. The mounted samples were gradually ground using SiC papers up to 2500 grit. The ground samples were then polished using a 0.05  $\mu\text{m}$  SiC suspension. Moreover, in order to reveal microstructural features such as cellular dendrites, the grain structure, and various phases, the polished samples were etched using oxalic acid diluted with water at a 1:10 ratio. Electro-etching was carried out using a potential of 3–4 V for 5–10 s.

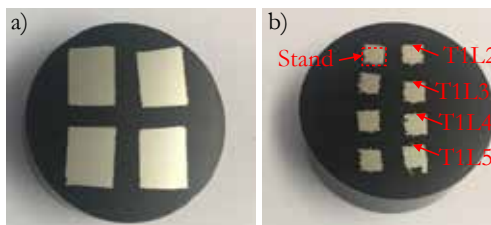


**Figure 3-8: Examples of the prepared samples: a) cross-section of the cubic samples, and b) cross-section of the layer-by-layer samples.**

For the transmission electron microscopy (TEM) examination in papers G and H, thin foils parallel to the build direction were prepared. In the first step, the samples were mechanically thinned to a thickness of approximately 100  $\mu\text{m}$ . Then, disks with a diameter of approximately 3 mm were punched out from the samples. The disks were further thinned mechanically to 10-20  $\mu\text{m}$  using a Gatan dimple grinder (model 656, Gatan Ltd., Corby, Northans, UK). Subsequently, ion beam milling was conducted on the thin samples to attain electron transparency using a Gatan precision ion polishing system (model 691, Gatan Ltd., Corby, Northans, UK).

For small-angle X-ray scattering (SAXS) in paper H, very thin foils with a thickness below 50  $\mu\text{m}$  were prepared, and eight points per foil were examined.

### **3.4 Characterization techniques and measurements**

#### **3.4.1 Light optical microscopy**

Two LOM, that is, Olympus (BX60M, Tokyo, Japan) and Zeiss (Axio Imager 2, Cambridge, UK) were utilized to observe the type of defects and to identify the characteristics of the melt pool geometry, for example, the melt pool depth, melt pool width, contact angle, and track height. LOM was used in almost all the studies.

#### **3.4.2 Scanning electron microscopy**

A Hitachi scanning electron microscope (TM3000, Tokyo, Japan) equipped with an EDS (Cambridge, UK) was used to characterize the chemical composition of the different phases; the microscope was typically operated at 15–20 kV in the backscatter electron mode (BSE). Using scanning electron microscope, the microstructural features, such as the primary dendrite arm spacing (PDAS), and different phases such as the niobium-rich carbides, were identified. A Zeiss scanning electron microscope (EVO 50, Oxford, the United Kingdom), and a Tescan scanning electron microscope (GAIA3, Oxford, United Kingdom) were also used to examine the solidification mode and the corresponding phase constituents, such as the  $\delta$  phase (in case of its presence). EDS analysis was performed to identify the elemental distribution in different phases.

#### **3.4.3 Electron backscattered diffraction**

A Tescan SEM coupled with an electron backscattered diffraction (EBSD) (GAIA3, Oxford, United Kingdom) detector operating at an accelerating voltage of 20 kV was used to investigate the grain orientation.

### 3.4.4 X-ray computed tomography

X-ray computed tomography was conducted using a Zeiss Xradia 520 Versa (Zeiss, Oberkochen, Germany) at 140 kV and 10 W with an exposure time of 1 s per 2D slice to capture the 3D vision of the cracks and shrinkage pores in papers G and H. The 2D projections were reconstructed to a 3D image using a beam hardening of 0.05 and analyzed in Dragonfly 3.1 (Object Research Systems, Montreal, Canada).

### 3.4.5 Transmission electron microscopy

A JEOL transmission electron microscope (JEOL, JEM. 2010F, Tokyo, Japan) operating at an accelerating voltage of 200 kV was used to characterize the precipitates in the thin foils. The size of the precipitates was estimated using an image analysis technique. For each sample in papers G and H, at least five TEM images were used to provide a proper estimation of the size of the  $\gamma''$  precipitates. Furthermore, selected area diffraction was performed to determine the crystal structure of the  $\gamma$  matrix and the  $\gamma''$  precipitates.

### 3.4.6 Small-angle X-ray scattering

A SAXS (SAXSLab Mat:Nordic, Denmark) instrument with a Rigaku 003+ high brilliance microfocus Cu-radiation source was used to quantitatively analyze the size of the  $\gamma''$  precipitates in different conditions in paper H. The size of  $\gamma''$  was extracted and reported as the radius of gyration based on the Guinier approximation.

### 3.4.7 Hardness test

Hardness measurements were carried out in all the studies using a Shimadzu HMV-2 micro Vickers hardness tester. The load was set to 500 g, and the dwell time was 15 s.

### 3.4.8 Defect measurement

For each cubic sample, 16–25 LOM images were taken in the normal reference plane (parallel to the build direction) to examine the defects, such as porosity, LoF defects, cracks, and shrinkage pores. The porosity measurement was performed using the point-counting method according to the ASTM E562-08 standard [112] on optical micrographs with a horizontal field width of 500  $\mu\text{m}$ . In the point-counting method, the images were first gridded with a pre-defined grid size (with

1540 crosses), then the areas with black spots that overlapped with the crosses were counted.

Moreover, 16 LOM images with a horizontal field width of 2.5 mm were taken from each sample and measured via the image analysis technique using ImageJ software [113] to determine the average total crack and total shrinkage length.

### 3.4.9 Quantification of niobium-rich phases

The presence of niobium-rich phases was measured using the point-counting method. Five to ten SEM images with a horizontal field width of 60 μm were used to quantify this phase. Figure 3-9 shows the grid pattern on an SEM image. In this method, the white particles were confirmed by EDS to be rich in niobium, as heavier elements absorb higher energies during the SEM observation.

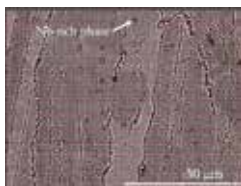


**Figure 3-9: SEM (BSE mode) image with gridding for point counting of the niobium-rich carbide.**

### 3.4.10 Primary dendrite arm spacing

Figure 3-10 illustrates the approach used to measure the PDAS using Eq. 2 [114], and SEM images with a horizontal field width of 45 μm. Depending on the surface area of the cross-sections, 5–10 SEM images were used for the measurement.

$$PDAS = \frac{L}{n} \tag{2}$$

where L is the length from the middle of one arm to the middle of the other arm, and n is the number of arms.

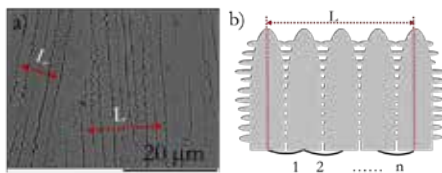


**Figure 3-10: a) SEM (BSE mode) image of the dendritic structure, and b) a schematic view of the dendrites.**

## 4 Summary of the appended papers

### Paper A: Microstructure development in track-by-track melting of EBM-manufactured Alloy 718

**Author contribution:** As the main and corresponding author, Paria Karimi performed all the experimental characterizations, analyzed all the results, and developed the structure of the paper. She was chiefly responsible for writing the paper. The coauthors contributed to formulating concepts and ideas, planning the project, manufacturing the samples, and reviewing the paper.

**Connection to the research questions:** This paper is related to the microstructural evolution of Alloy 718 within a single layer during the EB-PBF process, which is a part of RQ1 (refer to Section 1.1).

**Summary:** The aim of this study was to gain an increased fundamental understanding of the relationship between the geometry-related parameters and the microstructure formed within a single layer. Hence, different numbers of tracks of equal heights were produced using the same machine-related parameters for this purpose, varying from one to ten. The microstructural characteristics (grain structures and phases) were analyzed using different characterization techniques. The deposited tracks became a continuous solid material after adding three tracks next to each other using a constant scanning speed and current along the track. The direction of the dendrites in the overlap zone changed by approximately  $90^\circ$  from the build direction, towards either the adjacent track or the scanning direction. The cross-sections of the EB-PBF manufactured samples showed epitaxial growth of the columnar grains with a strong  $\langle 100 \rangle$  texture from the underlying layers and the nucleation of fine elongated grains in the overlap zones. In addition, small equiaxed grains on the surface of the tracks were also observed, which were most likely a result of the heat radiated from the surface. The coarsening of the new grains in the overlap zone relative to the new grains on the surfaces of the tracks was an indication of the slightly slower cooling rate in the overlap zone than in the rest of the track, which is due to double beam exposure and the resulting slower heat dissipation. Characterization of the PDAS in different tracks for each sample showed slight increases in the PDAS along a single layer, and subsequently, the cooling rate was estimated to be in the range of  $0.6 \times 10^5$ – $3 \times 10^5$  K/s.

## **Paper B: Influence of successive thermal cycling on microstructure evolution of EBM-manufactured Alloy 718 in track-by-track and layer-by-layer design**

**Author contribution:** As the main and corresponding author, Paria Karimi performed all the experimental characterizations, analyzed all the results, and developed the structure of the paper. She was chiefly responsible for writing the paper. The coauthors contributed to formulating concepts and ideas, planning the project, manufacturing the samples, and reviewing the paper.

**Connection to the RQs:** The aim of this study was to explore the effect of successive thermal cycling resulting from geometry-related parameters on the microstructural characteristics of EB-PBF manufactured Alloy 718, which is related to RQ1 (refer to Section 1.1).

**Summary:** The aim of this study was to determine the effects of successive thermal cycling (STC) during the multitrack and multilayer manufacturing of Alloy 718 via EB-PBF. Therefore, samples composed of a single track to 3D samples with a maximum of 10 longitudinal tracks, and 50 vertical layers were manufactured. The relationship between STC, solidification microstructure, interdendritic segregation, phase precipitation (MC-type carbide, and  $\delta$  phase), and hardness was investigated. The cooling rates (for the liquid-to-solid and solid-to-solid transformations) were estimated by measuring the PDAS. The PDAS values were higher at the bottom than the top of the multilayer samples. As a comparison, in the sample with 25 layers, PDAS was  $1.96 \pm 0.22 \mu\text{m}$  for the bottom region and  $2.94 \pm 0.31 \mu\text{m}$  for the top region. Thus, a microstructural gradient was identified along the build direction. Moreover, the extensive formation of solidification micro-constituents, including MC-type carbides, which are formed by microsegregation, was observed in all the samples. The EBSD technique revealed a highly textured structure along the  $\langle 100 \rangle$  direction, with a few grains misoriented at the surfaces of all the samples. The finer microstructure observed at the bottom of the samples resulted in higher (approximately 11 %) hardness values compared to the top of the samples.

## SUMMARY OF THE APPENDED PAPERS

### **Paper C: Influence of build layout and orientation on microstructural characteristics of electron beam melted Alloy 718**

**Author contribution:** As the main and corresponding author, Paria Karimi performed all the experimental characterizations, analyzed all the results, and developed the structure of the paper. She was chiefly responsible for writing the paper. The coauthors contributed to formulating concepts and ideas, planning the project, manufacturing the samples, and reviewing the paper.

**Connection to the research questions:** This study aimed to determine how the position-related parameters affect the microstructure of Alloy 718 during the EB-PBF process, which is related to RQ2 (refer to Section 1.1).

**Summary:** The effects of critical position-related parameters consisting of: a) height from the build plate (Z-axis), b) distance between samples, and c) location in the build plate (X-Y plane) on the porosity, NbC fraction, and hardness were studied. The as-built samples predominantly showed a columnar structure with a strong  $\langle 100 \rangle$  crystallographic orientation parallel to the build direction as well as NbC and  $\delta$  phases in the interdendritic regions and at the grain boundaries. Increasing the distance from the build plate led to the formation of a predominant columnar microstructure. The fine grains were found to be fewer in the samples built with a higher height from the build plate. By increasing the height to 45 mm from the build plate, the formation of the  $\delta$  phase was enhanced. Moreover, by increasing the height, the NbC fraction increased by approximately 116%, and the hardness increased slightly by approximately 6%, but the porosity fraction did not vary significantly. By increasing the sample gap (from 2 to 10 mm), no significant effect was found for the NbC fraction and hardness, but in the larger sample gap, the porosity fraction was increased by approximately 94%. The effect of the sample location on the porosity was evident, in which the former decreased in the exterior sample, whereas the latter increased; however, its effect on the NbC fraction and hardness was insignificant.

## **Paper D: Effect of build location on microstructural characteristics and corrosion behavior of EB-PBF-built Alloy 718**

**Author contribution:** As the main and corresponding author, Paria Karimi performed all the experimental characterizations, analyzed all the results, and developed the structure of the paper. She was chiefly responsible for writing the paper. The coauthors contributed to formulating concepts and ideas, planning the project, manufacturing the samples, and reviewing the paper article.

**Connection to the RQs:** Due to the unknown effects of part location in paper C, this paper aims to determine how the part location could affect the microstructural characteristics of Alloy 718 during the EB-PBF process, which is related to RQ2 (refer to Section 1.1).

**Summary:** Variations in the microstructure and corrosion performance as a function of the location of the parts on the build plate were investigated. The microstructural features were correlated with the thermal history of the samples built in different locations on the build plate, including exterior (outermost), middle (between the outermost and innermost), and interior (the innermost) regions. The columnar grains parallel to the build direction had strong texture in the  $\langle 001 \rangle$  direction and were observed in all the samples manufactured at different locations. Slightly more stray grains were formed in the samples located in the exterior region. The cubic samples located in the exterior regions showed an increased amount (approximately 20%) of defects (mainly in the form of shrinkage pores) and a lower level (approximately 30–35%) of the Nb-rich phase fraction due to their higher cooling rates compared to the interior and middle samples. The PDAS was measured and found to be coarser (approximately 20–30%) in the samples located in the interior region. Microhardness did not show any clear trend in the samples manufactured at different locations. Electrochemical investigations showed that the location indirectly had a substantial influence on the corrosion behavior, verified by a significant increase in polarization resistance ( $R_p$ ) from the exterior ( $2.1 \pm 0.3 \text{ k}\Omega\cdot\text{cm}^2$ ) to interior regions ( $39.2 \pm 4.1 \text{ k}\Omega\cdot\text{cm}^2$ ).

## SUMMARY OF THE APPENDED PAPERS

### **Paper E: EBM-manufactured single tracks of Alloy 718: Influence of energy input and focus offset on geometrical and microstructural characteristics**

**Author contribution:** As the main and corresponding author, Paria Karimi performed all the experimental characterizations, analyzed all the results, and developed the structure of the paper. She was chiefly responsible for writing the paper. The coauthors contributed to formulating concepts and ideas, planning the project, manufacturing the samples, and reviewing the paper.

**Connection to the research questions:** This paper focuses on identifying how machine-related parameters influence the microstructural characteristics of EB-PBF manufactured Alloy 718, which is related to RQ3 (refer to Section 1.1).

**Summary:** Linear energy input parameters, including beam scanning speed, beam current, and focus offset, and their effects on the geometry and microstructure of EB-PBF manufactured single tracks of Alloy 718 were analyzed. An increased scanning speed led to lower linear energy input values ( $<0.90$  J/mm) in a specific range of focus offsets (0–10 mA), which resulted in the instability and discontinuity of the single tracks as well as a balling effect. Decreasing the scanning speed and increasing the beam current resulted in a larger melt pool depth and width. Through statistical evaluation, the parameters that were most influential on the geometric features were determined to be the scanning speed first and the beam current second. The PDAS decreased significantly upon increasing the scanning speed for lower beam current values. By increasing the linear energy input, the probability of obtaining more equiaxed grains was high; in contrast, with lower linear energy input, an increased amount of columnar grains was observed. In addition, a lower focus offset resulted in a more uniform grain structure.

## **Paper F: Contour design to improve topographical and microstructural characteristics of Alloy 718 manufactured by electron beam-powder bed fusion technique**

**Author contribution:** As the main and corresponding author, Paria Karimi performed all the experimental characterizations, analyzed all the results, and developed the structure of the paper. She was chiefly responsible for writing the paper. The coauthors contributed to formulating concepts and ideas, planning the project, manufacturing the samples, and reviewing the paper.

**Connection to the research questions:** This paper focuses on identifying how the machine-related parameters affect the internal and external features of EB-PBF manufactured Alloy 718, which is related to RQ3 (refer to Section 1.1).

**Summary:** The effects of some critical machine-related parameters of the EB-PBF technique—such as scanning speed, beam current, focus offset, and the number of contours (one or two), as well as the linear melting strategy—on the surface roughness, geometrical accuracy, defect content, and grain morphology in the contour region were investigated. A sample manufactured using Arcam recommended process parameters (three contours with a spot melting strategy) was used for reference. Regarding the surface roughness, for the samples with one contour, the scanning speed had the greatest effect on the arithmetical mean height ( $S_a$ ), and for the samples with two contours, the beam current and focus offset had the greatest effect. For the samples with two contours, a lower focus offset and lower scanning speed (at a higher beam current) resulted in a lower  $S_a$ ; however, increasing the scanning speed for the samples with one contour decreased  $S_a$ . Moreover, the lowest surface roughness reached using the linear melting strategy was approximately 50  $\mu\text{m}$ . Fewer defects were also detected with a lower scanning speed and higher beam current. The focus offset and beam current had significant effects on the porosity fraction in the samples with two contours. Therefore, in general, the samples with two contours provided a lower  $S_a$  (approximately 22%), but with slightly higher porosity (approximately 8%) compared to the samples with one contour. The number of defects and the  $S_a$  value for the samples with two contours manufactured using the linear melting strategy were approximately 85% and 16%, respectively, lower than those of the reference samples manufactured using the spot melting strategy. The most influential parameter for the geometrical features was the scanning speed, which was followed by the beam current, and the focus offset was found to have a quantitatively insignificant effect. The linear melting strategy resulted in a larger deviation from the CAD model compared to the spot melting strategy in the Arcam reference sample. More columnar grains were observed in the contour regions when using linear melting than when using the spot melting strategy. In the samples with two contours, more columnar grains were observed compared to the samples with one contour.

## SUMMARY OF THE APPENDED PAPERS

### **Paper G: Columnar-to-equiaxed transition in powder bed fusion by mimicking casting solidification and promoting *in situ* recrystallization**

**Author contribution:** As the main and corresponding author, Paria Karimi performed all the experimental characterizations, analyzed all the results, and developed the structure of the paper. She was chiefly responsible for writing the paper. The coauthors contributed to formulating concepts and ideas, planning the project, manufacturing the samples, and reviewing the paper.

**Connection to the research questions:** This paper focuses on answering how the microstructure of Alloy 718 in the EB-PBF process can be tailored, which is related to RQ4 (refer to Section 1.1).

**Summary:** Using a novel melting strategy, the casting solidification conditions in EB-PBF were mimicked to promote *in situ* recrystallization, leading to the columnar-to-equiaxed grain transition. This was realized via a unique linear melting strategy coupled with a specific process window in EB-PBF. It induced casting solidification conditions as well as *in situ* recrystallization in the as-solidified grains and at the grain boundaries. The solidification parameter transition mechanism was explored. It was found that the line order number affects the cooling rate and temperature gradient, which determine the grain morphology and texture. An increase in the line order number provided the required solidification conditions to create a microstructure similar to the as-cast microstructure. A line order number increase from one to ten resulted in a remarkable reduction in the texture and columnar-to-equiaxed grain structure transition as well as an increase in the cooling rate in the local solidification conditions. In the proposed melting strategy, solidification cracking and shrinkage pores were observed in the samples. Variation in the grain boundary energy between the low- and high-angle grain boundaries affected the crack stability. The high-angle grain boundaries were more susceptible to cracking. The application of thermal stress during solidification resulted in shrinkage pore formation. Using the novel scanning strategy, increasing the line order number reduced crack formation and shrinkage defects. The size of the  $\gamma''$  precipitates decreased during the columnar-to-equiaxed grain structure transition, leading to lower hardness values.

## **Paper H: Tailored grain morphology via a novel double melting strategy in electron beam-powder bed fusion**

**Author contribution:** As the main and corresponding author, Paria Karimi performed all the experimental characterizations, analyzed all the results, and developed the structure of the paper. She was chiefly responsible for writing the paper. The coauthors contributed to formulating concepts and ideas, planning the project, manufacturing the samples, and reviewing the paper.

**Connection to the research questions:** This paper also focuses on identifying how the microstructure of Alloy 718 in the EB-PBF process can be tailored, which is related to RQ4 (refer to Section 1.1).

**Summary:** The double melting of each layer during EB-PBF was developed as a novel approach to tailoring the grain morphology of Alloy 718. The scanning speed (400–800 mm/s), line offset (300–500  $\mu\text{m}$ ), beam current (10–15 mA), and constant number of line orders (#10) were investigated to induce more vigorous movement and local solidification conditions in melt pools to tailor the grain morphology. Four different types of microstructure were classified according to the grain morphology—fully columnar, fully equiaxed, mixed columnar-equiaxed grains, and hemispherical melt pools containing mixed columnar-equiaxed grains were observed. The reduction of the overlap zone between two adjacent melt pools to approximately 20–25% facilitated the formation of the hemispherical melt pools containing mixed columnar-equiaxed grains. An overlap of less than 15% between two adjacent melt pools led to the formation of fully equiaxed grains. When the overlap was above 40%, either a columnar or mixed morphology was formed. The main reasons for the transition were 1) the reduction of the overlaps between the melt pools and 2) the remelting depth, which helped to block the epitaxial grain growth by altering the thermal gradient direction. Along with the tailored grain structure, long strings of shrinkage pores and cracks were also observed. The grain boundary energy, which varied significantly between low- and high-angle grain boundaries, was recognized as a factor that could facilitate cracking. Increasing the applied area energy input at different values of the line offsets increased the total number of shrinkage pores and cracks. The typical texture was  $\langle 001 \rangle$ ; however, the texture was reduced through the columnar-to-equiaxed grain structure transition. The hardness increased through the transition, which was linked to an increase in the size of the  $\gamma''$  precipitates.

## 5 Conclusions

The influence of the process parameters on microstructural characteristics in the electron beam-powder bed fusion of Alloy 718 was examined. In this thesis, the process parameters were divided into three categories—geometry-, position-, and machine-related parameters. The conclusions are divided into four parts based on the RQs:

### **Understanding the evolution of microstructural characteristics through geometry-related parameters (RQ1):**

-Through a closer inspection of microstructural evolution via different geometries, the influence of STC on the microstructural features was investigated. The PDAS was slightly coarser in the overlap zone compared to the area of the track that had been melted only once. This indicates a slightly lower cooling rate in the overlap zone than in the rest of the track. The characterization of the PDAS in different tracks for each sample showed a slight increase in PDAS widths by increasing the number of tracks, which indicated that the cooling rate decreased with the addition of tracks along the same layer. In addition, a slightly higher cooling rate was observed at the bottom than in the top layers. Moreover, by increasing the wall thickness, the cooling rate was reduced. The hardness profile along the walls (both single and thick walls) revealed slightly higher values (approximately 11%) for the bottom layers compared to the more elevated layers, owing to the finer microstructure of the bottom layers.

### **Effect of position-related parameters on microstructural characteristics (RQ2):**

-The orientation/position of the parts on the build plate during the EB-PBF process can have significant effects on the microstructural characteristics. This could be attributed to the different thermal mass/heat accumulations observed during the melting of the part, which can lead to different solidification parameters and, subsequently, different microstructures. The content of defects (mainly LoF), phase fractions, and grain structure were changed using different position-related parameters. In addition, for lower sample gaps, the content of defects decreased. Finally, upon elevating the parts relative to the build plate and accordingly reducing the cooling rate, the niobium segregation was increased, which led to the precipitation of the  $\delta$  phase. Slightly more stray grains were formed in the samples located in the exterior region. The parts in the exterior

regions showed an increased level of defects (mainly in the form of shrinkage pores) and lower levels of the niobium-rich phase fraction due to their higher cooling rates compared to the parts in the interior and middle regions.

### **Influence of machine-related parameters on internal and external features (RQ3)**

-The effects of the three critical machine-related parameters (scanning speed, beam current, and focus offset) and their interactions with the geometrical and microstructural features of the single tracks were investigated. At lower linear energy input values, the risk of discontinuous tracks and instability was the highest. The most influential parameter of the geometrical features was the scanning speed, followed by the beam current. Compared to the other two parameters, the focus offset was found to have a quantitative effect on the geometrical features. Moreover, by increasing the linear energy input value, the probability of obtaining more equiaxed grains was high; in contrast, for a lower linear energy input value, more columnar grains were observed. A lower focus offset resulted in reduced misorientation within the grains. The results of this single-track study were used to improve the external (surface roughness) and internal defects (pores, LoF, etc.) in the as-built condition. It was found that the surface roughness and defect content were significantly better when using the linear melting strategy and two contours using the optimized set of process parameters compared to the Arcam-recommend process parameters for the contour region. The lowest surface roughness ( $S_a$ ) obtained using the linear melting strategy was 50  $\mu\text{m}$ .

### **Proposed melting strategies for tailoring microstructure (RQ4):**

-Two different melting strategies were proposed to facilitate the columnar-to-equiaxed grain structure transition. One approach was to use the line order number function with a very tight line offset and high scanning speed to mimic the cast solidification behavior and promote *in situ* recrystallization. A higher line order number provided the solidification conditions required to create a microstructure similar to the as-cast microstructure. Thus, by increasing the line order number, a remarkable reduction in the texture and columnar-to-equiaxed grain structure transition was attained. Moreover, the size of the  $\gamma''$  precipitates decreased during the columnar-to-equiaxed grain structure transition. Solidification cracking and shrinkage pores were observed due to variation in the grain boundary energy between low and high-angle grain boundaries (more susceptible to cracking). Increasing the line order number reduced the crack formation and shrinkage defects.

The second melting strategy, known as a double melting strategy, showed a reduction in the overlap zone between the melt pools/scan lines and the remelting

## CONCLUSIONS

depth, facilitating the blockage of epitaxial grain growth by altering the thermal gradient direction and cooling rate. The size of the  $\gamma''$  precipitates increased during the columnar-to-equiaxed grain structure transition. Moreover, the numbers of cracks and shrinkage defects were reduced by increasing the scanning speed and line offset.



## 6 Future research

Additional research is required to determine the effects of other position-related parameters such as part angle on the microstructural characteristics of EB-PBF manufactured Alloy 718.

-Further evaluation of the influence of machine-related parameters on microstructural characteristics can be of great interest. A limited number of machine-related parameters with a specific range has been investigated so far; however, the outer frame of the parameter ranges needs to be analyzed to establish a broader window. In addition, parameters such as layer thickness need to be investigated to understand the effects of these parameters on microstructural features such as internal and external defects.

-Herein, two different melting strategies were proposed for tailoring the grain structure; however, there are other approaches that need to be investigated for this purpose. In addition, the mechanical properties of tailored microstructures, such as fatigue, will be of great interest.

-In this study, tailoring the grain structure led to the formation of cracks in the as-built material. More process parameters need to be investigated to eliminate the formation of cracks. In addition, post-processing, such as hot isostatic pressing, can be applied to heal the cracks with minimal changes in the obtained grain morphologies.



## References

- [1] S. C. Joshi and A. A. Sheikh, “3D printing in aerospace and its long-term sustainability,” *Virtual Phys. Prototyp.*, vol. 10, no. 4, pp. 175–185, Oct. 2015, doi: 10.1080/17452759.2015.1111519.
- [2] “Global Aerospace Additive Manufacturing Industry.” [https://www.reportlinker.com/p05797787/Global-Aerospace-Additive-Manufacturing-Industry.html?utm\\_source=PRN](https://www.reportlinker.com/p05797787/Global-Aerospace-Additive-Manufacturing-Industry.html?utm_source=PRN) (accessed Jun. 18, 2020).
- [3] S. Reichelt, T. Mertens, D. Greitemeier, L. Carton, and A. Schoberth, “Surface finishing of additive manufactured Ti-6Al-4V – a comparison of electrochemical and mechanical treatments,” presented at the 6th European conference for aerospace science, Krakau, Poland, Jun. 2015.
- [4] J. Karlsson, “Optimization of Electron Beam Melting for Production of Small Components in Biocompatible Titanium Grades,” Doctoral thesis, University of Uppsala, 2015.
- [5] V. Bhavar, P. Kattire, V. Patil, S. Khot, K. Gujar, and R. R. Singh, “A Review on Powder Bed Fusion Technology of Metal Additive Manufacturing,” presented at the 4th International conference and exhibition on Additive Manufacturing Technologies-AM-2014, Bangalore, India., Sep. 2014.
- [6] W. Sames, “Additive Manufacturing of Inconel 718 using Electron Beam Melting: Processing, Post-Processing, & Mechanical Properties,” Doctoral thesis, 2015.
- [7] L. E. Murr, S. M. Gaytan, E. Martinez, and F. R. Medina, “Metal Fabrication by Additive Manufacturing Using Laser and Electron Beam Melting Technologies,” *J. Mater. Sci. Technol.*, vol. 28, no. 1, pp. 1–14, Jan. 2012, doi: 10.1016/S1005-0302(12)60016-4.
- [8] W. Gao, Y. Zhang, D. Ramanujan, K. Ramani, and Y. Chen, “The status, challenges, and future of additive manufacturing in engineering,” *Comput.-Aided Des.*, vol. 69, pp. 65–89, Dec. 2015, doi: 10.1016/j.cad.2015.04.001.
- [9] X. Wang, X. Gong, and K. Chou, “Review on powder-bed laser additive manufacturing of Inconel 718 parts,” *Proc. Inst. Mech. Eng. Part B J. Eng. Manuf.*, vol. 231, no. 11, pp. 1890–1903, Sep. 2017, doi: 10.1177/0954405415619883.
- [10] Y. Lee, “Simulation of Laser Additive Manufacturing and its Applications,” Doctoral thesis, The Ohio State University, 2015.
- [11] L. Sheridan, “An Adapted Approach to Process Mapping across Alloy Systems and Additive Manufacturing Processes,” Master thesis, Wright State University, 2016.
- [12] N. Guo and M. C. Leu, “Additive manufacturing: technology, applications and research needs,” *Front. Mech. Eng.*, vol. 8, no. 3, pp. 215–243, Sep. 2013, doi: 10.1007/s11465-013-0248-8.
- [13] R. Hague, S. Mansour, and N. Saleh, “Material and design considerations for rapid manufacturing,” *Int. J. Prod. Res.*, vol. 42, no. 22, pp. 4691–4708, Nov. 2004, doi: 10.1080/00207840410001733940.

- [14] S. Mellor, L. Hao, and D. Zhang, "Additive manufacturing: A framework for implementation," *Int. J. Prod. Econ.*, vol. 149, pp. 194–201, Mar. 2014, doi: 10.1016/j.ijpe.2013.07.008.
- [15] S. Gorsse, C. Hutchinson, M. Gouné, and R. Banerjee, "Additive manufacturing of metals: a brief review of the characteristic microstructures and properties of steels, Ti-6Al-4V and high-entropy alloys," *Sci. Technol. Adv. Mater.*, vol. 18, no. 1, pp. 584–610, Dec. 2017, doi: 10.1080/14686996.2017.1361305.
- [16] J. Holmström, J. Partanen, J. Tuomi, and M. Walter, "Rapid manufacturing in the spare parts supply chain: Alternative approaches to capacity deployment," *J. Manuf. Technol. Manag.*, vol. 21, no. 6, pp. 687–697, Jul. 2010, doi: 10.1108/17410381011063996.
- [17] "Additive Manufacturing: Pursuing the Promise," U.S. Department of ENERGY, USA, Aug. 2012.
- [18] A. A. Antonyamy, "Microstructure, Texture and Mechanical Property Evolution During Additive Manufacturing of Ti6Al4V Alloy for Aerospace Applications," Doctoral thesis, University of Manchester, 2012.
- [19] Y. H. Kok, X. P. Tan, N. H. Loh, S. B. Tor, and C. K. Chua, "Geometry dependence of microstructure and microhardness for selective electron beam-melted Ti-6Al-4V parts," *Virtual Phys. Prototyp.*, vol. 11, no. 3, pp. 183–191, Jul. 2016, doi: 10.1080/17452759.2016.1210483.
- [20] J. K. Algardh *et al.*, "Thickness dependency of mechanical properties for thin-walled titanium parts manufactured by Electron Beam Melting (EBM)," *Addit. Manuf.*, vol. 12, pp. 45–50, Oct. 2016, doi: 10.1016/j.addma.2016.06.009.
- [21] N. Hrabe and T. Quinn, "Effects of processing on microstructure and mechanical properties of a titanium alloy (Ti-6Al-4V) fabricated using electron beam melting (EBM), part 1: Distance from build plate and part size," *Mater. Sci. Eng. A*, vol. 573, pp. 264–270, Jun. 2013, doi: 10.1016/j.msea.2013.02.064.
- [22] N. Hrabe and T. Quinn, "Effects of processing on microstructure and mechanical properties of a titanium alloy (Ti-6Al-4V) fabricated using electron beam melting (EBM), Part 2: Energy input, orientation, and location," *Mater. Sci. Eng. A*, vol. Complete, no. 573, pp. 271–277, 2013, doi: 10.1016/j.msea.2013.02.065.
- [23] R. M. Mahamood, E. T. Akinlabi, M. Shukla, and S. Pityana, "Revolutionary additive manufacturing: An overview," *Lasers Eng.*, vol. 27, no. 3–4, pp. 161–178, 2014.
- [24] P. Wang, W. J. Sin, M. L. S. Nai, and J. Wei, "Effects of Processing Parameters on Surface Roughness of Additive Manufactured Ti-6Al-4V via Electron Beam Melting," *Mater. Basel Switz.*, vol. 10, no. 10, Sep. 2017, doi: 10.3390/ma10101121.
- [25] C. J. Smith *et al.*, "Dimensional accuracy of Electron Beam Melting (EBM) additive manufacture with regard to weight optimized truss structures," *J. Mater. Process. Technol.*, vol. 229, pp. 128–138, Mar. 2016, doi: 10.1016/j.jmatprotec.2015.08.028.
- [26] A. Segerstark, "Additive Manufacturing using Alloy 718 Powder: Influence of Laser Metal Deposition Process Parameters on Microstructural Characteristics," Doctoral thesis, University West, 2015.
- [27] T. DebRoy *et al.*, "Additive manufacturing of metallic components – Process, structure and properties," *Prog. Mater. Sci.*, vol. 92, pp. 112–224, Mar. 2018, doi: 10.1016/j.pmatsci.2017.10.001.

## REFERENCES

- [28] S. Mohd Yusuf, S. Cutler, and N. Gao, "Review: The Impact of Metal Additive Manufacturing on the Aerospace Industry," *Metals*, vol. 9, no. 12, Art. no. 12, Dec. 2019, doi: 10.3390/met9121286.
- [29] S. Kumar, "Electron Beam Powder Bed Fusion," in *Additive Manufacturing Processes*, S. Kumar, Ed. Cham: Springer International Publishing, 2020, pp. 65–78.
- [30] N. Hrabe and T. Quinn, "Effects of processing on microstructure and mechanical properties of a titanium alloy (Ti–6Al–4V) fabricated using electron beam melting (EBM), part 1: Distance from build plate and part size," *Mater. Sci. Eng. A*, vol. 573, pp. 264–270, Jun. 2013, doi: 10.1016/j.msea.2013.02.064.
- [31] S. Anwar, N. Ahmed, B. M. Abdo, S. Pervaiz, M. A. K. Chowdhury, and A. M. Alahmari, "Electron beam melting of gamma titanium aluminide and investigating the effect of EBM layer orientation on milling performance," *Int. J. Adv. Manuf. Technol.*, vol. 96, no. 9, pp. 3093–3107, Jun. 2018, doi: 10.1007/s00170-018-1802-7.
- [32] M. M. Kirka, K. A. Unocic, N. Raghavan, F. Medina, R. R. Dehoff, and S. S. Babu, "Microstructure Development in Electron Beam-Melted Inconel 718 and Associated Tensile Properties," *JOM*, vol. 68, no. 3, pp. 1012–1020, Mar. 2016, doi: 10.1007/s11837-016-1812-6.
- [33] W. J. Sames, F. Medina, W. H. Peter, S. S. Babu, and R. R. Dehoff, "Effect of Process Control and Powder Quality on Inconel 718 Produced Using Electron Beam Melting," in *8th International Symposium on Superalloy 718 and Derivatives*, Wiley-Blackwell, 2014, pp. 409–423.
- [34] L. E. Murr, "Metallurgy of additive manufacturing: Examples from electron beam melting," *Addit. Manuf.*, vol. 5, pp. 40–53, Jan. 2015, doi: 10.1016/j.addma.2014.12.002.
- [35] L. E. Murr *et al.*, "Microstructures of Rene 142 nickel-based superalloy fabricated by electron beam melting," *Acta Mater.*, vol. 61, no. 11, pp. 4289–4296, Jun. 2013, doi: 10.1016/j.actamat.2013.04.002.
- [36] K. A. Unocic, M. M. Kirka, E. Cakmak, D. Greeley, A. O. Okello, and S. Dryepondt, "Evaluation of additive electron beam melting of haynes 282 alloy," *Mater. Sci. Eng. A*, vol. 772, p. 138607, Jan. 2020, doi: 10.1016/j.msea.2019.138607.
- [37] M. Romedenne, R. Pillai, M. Kirka, and S. Dryepondt, "High temperature air oxidation behavior of Hastelloy X processed by Electron Beam Melting (EBM) and Selective Laser Melting (SLM)," *Corros. Sci.*, vol. 171, p. 108647, Jul. 2020, doi: 10.1016/j.corsci.2020.108647.
- [38] M. A. Lodes, R. Guschlbauer, and C. Körner, "Process development for the manufacturing of 99.94% pure copper via selective electron beam melting," *Mater. Lett.*, vol. 143, pp. 298–301, Mar. 2015, doi: 10.1016/j.matlet.2014.12.105.
- [39] "Additive vacuum electronics: Electron beam melting of copper - IEEE Conference Publication." <https://ieeexplore.ieee.org/document/8289495> (accessed Sep. 24, 2020).
- [40] F. A. Shah *et al.*, "Long-term osseointegration of 3D printed CoCr constructs with an interconnected open-pore architecture prepared by electron beam melting," *Acta Biomater.*, vol. 36, pp. 296–309, May 2016, doi: 10.1016/j.actbio.2016.03.033.
- [41] C. Wang, X. Tan, E. Liu, and S. B. Tor, "Process parameter optimization and mechanical properties for additively manufactured stainless steel 316L parts by

- selective electron beam melting,” *Mater. Des.*, vol. 147, pp. 157–166, Jun. 2018, doi: 10.1016/j.matdes.2018.03.035.
- [42] Y. Zhong *et al.*, “Additive manufacturing of 316L stainless steel by electron beam melting for nuclear fusion applications,” *J. Nucl. Mater.*, vol. 486, pp. 234–245, 2017.
- [43] D. Cormier, O. Harrysson, and H. West, “Characterization of H13 steel produced via electron beam melting,” *Rapid Prototyp. J.*, vol. 10, no. 1, pp. 35–41, Feb. 2004, doi: 10.1108/13552540410512516.
- [44] P. D. Carrière, “Energy and charge transfer during electron beam melting,” 2018.
- [45] S. S. Al-Bermani, M. L. Blackmore, W. Zhang, and I. Todd, “The Origin of Microstructural Diversity, Texture, and Mechanical Properties in Electron Beam Melted Ti-6Al-4V,” *Metall. Mater. Trans. A*, vol. 41, no. 13, pp. 3422–3434, Dec. 2010, doi: 10.1007/s11661-010-0397-x.
- [46] C. Guo, W. Ge, and F. Lin, “Effects of scanning parameters on material deposition during Electron Beam Selective Melting of Ti-6Al-4V powder,” *J. Mater. Process. Technol.*, vol. 217, pp. 148–157, Mar. 2015, doi: 10.1016/j.jmatprotec.2014.11.010.
- [47] H. Hasib, O. L. A. Harrysson, and H. A. West, “Powder Removal from Ti-6Al-4V Cellular Structures Fabricated via Electron Beam Melting,” *JOM*, vol. 67, no. 3, pp. 639–646, Mar. 2015, doi: 10.1007/s11837-015-1307-x.
- [48] J. Karlsson, M. Norell, U. Ackelid, H. Engqvist, and J. Lausmaa, “Surface oxidation behavior of Ti-6Al-4V manufactured by Electron Beam Melting (EBM®),” *J. Manuf. Process.*, vol. 17, no. 1, pp. 120–126, 2015.
- [49] S. S. Al-Bermani, “An investigation into microstructure and microstructural control of additive layer manufactured Ti-6Al-4V by electron beam melting,” Doctoral thesis, University of Sheffield, 2011.
- [50] D. Kotzem, T. Arold, T. Niendorf, and F. Walther, “Influence of specimen position on the build platform on the mechanical properties of as-built direct aged electron beam melted Inconel 718 alloy,” *Mater. Sci. Eng. A*, vol. 772, p. 138785, Jan. 2020, doi: 10.1016/j.msea.2019.138785.
- [51] S. Goel, J. Olsson, M. Ahlfors, U. Klement, and S. Joshi, “The Effect of Location and Post-treatment on the Microstructure of EBM-Built Alloy 718,” in *Proceedings of the 9th International Symposium on Superalloy 718 & Derivatives: Energy, Aerospace, and Industrial Applications*, E. Ott, X. Liu, J. Andersson, Z. Bi, K. Bockenstedt, I. Dempster, J. Groh, K. Heck, P. Jablonski, M. Kaplan, D. Nagahama, and C. Sudbrack, Eds. Cham: Springer International Publishing, 2018, pp. 115–129.
- [52] P. Karimi, E. Sadeghi, J. Ålgårdh, P. Harlin, and J. Andersson, “Effect of build location on microstructural characteristics and corrosion behavior of EB-PBF built Alloy 718,” *Int. J. Adv. Manuf. Technol.*, vol. 106, no. 7, pp. 3597–3607, Feb. 2020, doi: 10.1007/s00170-019-04859-9.
- [53] P. Karimi, E. Sadeghi, D. Deng, H. Gruber, J. Andersson, and P. Nysten, “Influence of build layout and orientation on microstructural characteristics of electron beam melted Alloy 718,” *Int. J. Adv. Manuf. Technol.*, vol. 99, no. S1, pp. 2903–2913, 2018.
- [54] N. W. Hrabe, T. P. Quinn, and R. Kircher, “Effects of Processing on Microstructure and Mechanical Properties of Ti-6Al-4V Fabricated using Electron Beam Melting (EBM), Part 2: Energy Input, Orientation, and Location,” *Mater. Sci. Eng. -Struct. Mater. Prop. Microstruct. Process.*, vol. 573, Jun. 2013, Accessed: May 09,

## REFERENCES

2019. [Online]. Available: <https://www.nist.gov/publications/effects-processing-microstructure-and-mechanical-properties-ti-6al-4v-fabricated-0>.
- [55] A. A. Antonysamy, J. Meyer, and P. B. Prangnell, “Effect of build geometry on the  $\beta$ -grain structure and texture in additive manufacture of Ti6Al4V by selective electron beam melting,” *Mater. Charact.*, vol. 84, pp. 153–168, Oct. 2013, doi: 10.1016/j.matchar.2013.07.012.
- [56] J. Günther *et al.*, “Design of novel materials for additive manufacturing - Isotropic microstructure and high defect tolerance,” *Sci. Rep.*, vol. 8, no. 1, p. 1298, Jan. 2018, doi: 10.1038/s41598-018-19376-0.
- [57] H. E. Helmer, C. Körner, and R. F. Singer, “Additive manufacturing of nickel-based superalloy Inconel 718 by selective electron beam melting: Processing window and microstructure,” *J. Mater. Res.*, vol. 29, no. 17, pp. 1987–1996, Sep. 2014, doi: 10.1557/jmr.2014.192.
- [58] M. Galati and L. Iuliano, “A literature review of powder-based electron beam melting focusing on numerical simulations,” *Addit. Manuf.*, vol. 19, pp. 1–20, Jan. 2018, doi: 10.1016/j.addma.2017.11.001.
- [59] H. Helmer, A. Bauereiß, R. F. Singer, and C. Körner, “Grain structure evolution in Inconel 718 during selective electron beam melting,” *Mater. Sci. Eng. A*, vol. 668, no. Supplement C, pp. 180–187, Jun. 2016, doi: 10.1016/j.msea.2016.05.046.
- [60] P. Karimi Neghlani, “SLM additive manufacturing of Alloy 718 : effect of process parameters on microstructure and properties,” Master thesis, University West, 2016.
- [61] T. Scharowsky, V. Juechter, R. F. Singer, and C. Körner, “Influence of the Scanning Strategy on the Microstructure and Mechanical Properties in Selective Electron Beam Melting of Ti–6Al–4V,” *Adv. Eng. Mater.*, vol. 17, no. 11, pp. 1573–1578, Nov. 2015, doi: 10.1002/adem.201400542.
- [62] J. Andersson, “Weldability of Precipitation Hardening Superalloys – Influence of Microstructure,” Doctoral Thesis, Chalmers University, 2011.
- [63] C. T. Sims, Norman S. Stoloff, and William C. Hagel, *Wiley: Superalloys II: High-Temperature Materials for Aerospace and Industrial Power - Chester T. Sims, Norman S. Stoloff, William C. Hagel*. 1987.
- [64] R. C. Reed, *The Superalloys: Fundamentals and Applications*. Cambridge University Press, 2008.
- [65] H. X. Hu, Y. G. Zheng, and C. P. Qin, “Comparison of Inconel 625 and Inconel 600 in resistance to cavitation erosion and jet impingement erosion,” *Nucl. Eng. Des.*, vol. 240, no. 10, pp. 2721–2730, Oct. 2010, doi: 10.1016/j.nucengdes.2010.07.021.
- [66] J. W. Brooks and P. J. Bridges, “Metallurgical Stability of Inconel Alloy 718,” in *Superalloys 1988*, Jan. 1988, pp. 33–42, doi: 10.7449/1988/Superalloys\_1988\_33\_42.
- [67] D. F. Paulonis, J. J. Schirra, “Alloy 718 At Pratt & Whitney Historical Perspective And Future Challenges,” presented at the Superalloys 718, 625, 706 and Various Derivatives, USA, 2001, doi: 10.7449/2001/Superalloys\_2001\_13\_23.
- [68] S. Azadian, “Aspects of Precipitation in Alloy Inconel 718,” Doctoral thesis, University of Luleå, 2004.
- [69] A. Mitchell, “Primary Carbides in Alloy 718,” in *7th International symposium superalloy 718 and derivatives*, Pittsburgh, Pennsylvania, Oct. 2010, p. 7.

- [70] B. Geddes, H. Leon, and X. Huang, *Superalloys: Alloying and Performance*. ASM International, 2010.
- [71] D. R. Nielsen, S. W. Thompson, C. J. Van Tyne, and M. C. Mataya, “Grain Size Control in Ring-Rolled Alloy 718,” in *Superalloys 718, 625, 706 and Various Derivatives (1994)*, 1994, pp. 373–392, doi: 10.7449/1994/Superalloys\_1994\_373\_392.
- [72] W. J. Sames, F. A. List, S. Pannala, R. R. Dehoff, and S. S. Babu, “The metallurgy and processing science of metal additive manufacturing,” *Int. Mater. Rev.*, vol. 61, no. 5, pp. 315–360, Jul. 2016, doi: 10.1080/09506608.2015.1116649.
- [73] “smoking electron beam melting,” *Inside Metal Additive Manufacturing*. <http://www.insidemetaladditivemanufacturing.com/1/post/2016/06/smoking-effect-in-electron-beam-melting.html> (accessed Aug. 03, 2020).
- [74] X. Ding, Y. Koizumi, D. Wei, and A. Chiba, “Effect of process parameters on melt pool geometry and microstructure development for electron beam melting of IN718: A systematic single bead analysis study,” *Addit. Manuf.*, vol. 26, pp. 215–226, Mar. 2019, doi: 10.1016/j.addma.2018.12.018.
- [75] H.-J. Lee, H.-K. Kim, H.-U. Hong, and B.-S. Lee, “Influence of the focus offset on the defects, microstructure, and mechanical properties of an Inconel 718 superalloy fabricated by electron beam additive manufacturing,” *J. Alloys Compd.*, vol. 781, pp. 842–856, Apr. 2019, doi: 10.1016/j.jallcom.2018.12.070.
- [76] A. Strondl, R. Fischer, G. Frommeyer, and A. Schneider, “Investigations of MX and  $\gamma'/\gamma$  precipitates in the nickel-based superalloy 718 produced by electron beam melting,” *Mater. Sci. Eng. A*, vol. 480, no. 1–2, pp. 138–147, May 2008, doi: 10.1016/j.msea.2007.07.012.
- [77] A. Strondl, M. Palm, J. Gnauk, and G. Frommeyer, “Microstructure and mechanical properties of nickel based superalloy IN718 produced by rapid prototyping with electron beam melting (EBM),” *Mater. Sci. Technol.*, vol. 27, no. 5, pp. 876–883, May 2011, doi: 10.1179/026708309X12468927349451.
- [78] D. Deng, J. Saarimäki, H. Söderberg, R. Peng, H. Brodin, and J. Moverare, “Microstructural Characterization of AS-Manufactured and Heat Treated Electron Beam Melted Inconel 718,” 2016, pp. 105–112, Accessed: May 19, 2020. [Online]. Available: <http://urn.kb.se/resolve?urn=urn:nbn:se:liu:diva-132646>.
- [79] C. Körner, H. Helmer, A. Bauereiß, and R. F. Singer, “Tailoring the grain structure of IN718 during selective electron beam melting,” in *MATEC Web of Conferences*, Aug. 2014, vol. 14, p. 08001, doi: 10.1051/mateconf/20141408001.
- [80] M. M. Kirka, Y. Lee, D. A. Greeley, A. Okello, and R. R. Dehoff, “Strategy for Texture Management in Metals Additive Manufacturing,” *JOM*, vol. 69, no. 3, pp. 523–531, Mar. 2017, doi: 10.1007/s11837-017-2264-3.
- [81] M. M. Kirka, P. Nandwana, Y. Lee, and R. R. Dehoff, “Solidification and solid-state transformation sciences in metals additive manufacturing,” *Scr. Mater.*, vol. 135, pp. 130–134, Jul. 2017, doi: 10.1016/j.scriptamat.2017.01.005.
- [82] R. R. Dehoff, M. M. Kirka, F. A. List, K. A. Unocic, and W. J. Sames, “Crystallographic texture engineering through novel melt strategies via electron beam melting: Inconel 718,” *Mater. Sci. Technol.*, vol. 31, no. 8, pp. 939–944, Jun. 2015, doi: 10.1179/1743284714Y.0000000697.

## REFERENCES

- [83] R. R. Dehoff *et al.*, “Site specific control of crystallographic grain orientation through electron beam additive manufacturing,” *Mater. Sci. Technol.*, vol. 31, no. 8, pp. 931–938, Jun. 2015, doi: 10.1179/1743284714Y.0000000734.
- [84] N. Raghavan *et al.*, “Numerical modeling of heat-transfer and the influence of process parameters on tailoring the grain morphology of IN718 in electron beam additive manufacturing,” *Acta Mater.*, vol. 112, no. Supplement C, pp. 303–314, Jun. 2016, doi: 10.1016/j.actamat.2016.03.063.
- [85] E. Cakmak *et al.*, “Mechanical Characterization of an Additively Manufactured Inconel 718 Theta-Shaped Specimen,” *Metall. Mater. Trans. A*, vol. 47, no. 2, pp. 971–980, Feb. 2016, doi: 10.1007/s11661-015-3186-8.
- [86] S.-Y. Im *et al.*, “Unidirectional columnar microstructure and its effect on the enhanced creep resistance of selective electron beam melted Inconel 718,” *J. Alloys Compd.*, vol. 817, p. 153320, Mar. 2020, doi: 10.1016/j.jallcom.2019.153320.
- [87] S. Goel, M. Ahlfors, F. Bahbou, and S. Joshi, “Effect of Different Post-treatments on the Microstructure of EBM-Built Alloy 718,” *J. Mater. Eng. Perform.*, vol. 28, no. 2, pp. 673–680, Feb. 2019, doi: 10.1007/s11665-018-3712-0.
- [88] X. Ding *et al.*, “Microstructural control of alloy 718 fabricated by electron beam melting with expanded processing window by adaptive offset method,” *Mater. Sci. Eng. A*, vol. 764, p. 138058, Sep. 2019, doi: 10.1016/j.msea.2019.138058.
- [89] G. L. Knapp, N. Raghavan, A. Plotkowski, and T. DebRoy, “Experiments and simulations on solidification microstructure for Inconel 718 in powder bed fusion electron beam additive manufacturing,” *Addit. Manuf.*, vol. 25, pp. 511–521, Jan. 2019, doi: 10.1016/j.addma.2018.12.001.
- [90] W. J. Sames, K. A. Unocic, R. R. Dehoff, T. Lolla, and S. S. Babu, “Thermal effects on microstructural heterogeneity of Inconel 718 materials fabricated by electron beam melting,” *J. Mater. Res.*, vol. 29, no. 17, pp. 1920–1930, Sep. 2014, doi: 10.1557/jmr.2014.140.
- [91] W. J. Sames *et al.*, “Feasibility of in situ controlled heat treatment (ISHT) of Inconel 718 during electron beam melting additive manufacturing,” *Addit. Manuf.*, vol. 13, pp. 156–165, Jan. 2017, doi: 10.1016/j.addma.2016.09.001.
- [92] K. Kusabiraki, S. Ikeuchi, and T. Ooka, “Morphology and Lattice Constants of  $\gamma$ ” Precipitates in a Ni–18Cr–16Fe–5Nb–3Mo Alloy,” *Mater. Trans. JIM*, vol. 37, no. 5, pp. 1050–1055, 1996, doi: 10.2320/matertrans1989.37.1050.
- [93] M. C. Chaturvedi and Y. Han, “Strengthening mechanisms in Inconel 718 superalloy,” *Met. Sci.*, vol. 17, no. 3, pp. 145–149, Mar. 1983, doi: 10.1179/030634583790421032.
- [94] I. Kirman and D. H. Warrington, “The precipitation of Ni<sub>3</sub>Nb phases in a Ni–Fe–Cr–Nb alloy,” *Metall. Trans.*, vol. 1, no. 10, pp. 2667–2675, Oct. 1970, doi: 10.1007/BF03037800.
- [95] J. P. Collier, S. H. Wong, J. K. Tien, and J. C. Phillips, “The effect of varying Al, Ti, and Nb content on the phase stability of INCONEL 718,” *Metall. Trans. A*, vol. 19, no. 7, pp. 1657–1666, Jul. 1988, doi: 10.1007/BF02645133.
- [96] S. Azadian, L.-Y. Wei, and R. Warren, “Delta phase precipitation in Inconel 718,” *Mater. Charact.*, vol. 53, no. 1, pp. 7–16, Sep. 2004, doi: 10.1016/j.matchar.2004.07.004.

- [97] Y. Desvallees, M. Bouzidi, F. Bois, and N. Beaudé, “Delta Phase in INCONEL 718: Mechanical Properties and Forging Process Requirements,” 1994, pp. 281–291, doi: 10.7449/1994/Superalloys\_1994\_281\_291.
- [98] N. L. Richards, X. Huang, and M. C. Chaturvedi, “Heat affected zone cracking in cast inconel 718,” *Mater. Charact.*, vol. 28, no. 4, pp. 179–187, Jun. 1992, doi: 10.1016/1044-5803(92)90080-2.
- [99] Y. Mei *et al.*, “Effect of base metal and welding speed on fusion zone microstructure and HAZ hot-cracking of electron-beam welded Inconel 718,” *Mater. Des.*, vol. 89, pp. 964–977, Jan. 2016, doi: 10.1016/j.matdes.2015.10.082.
- [100] M. J. Donachie and S. J. Donachie, *Superalloys: A Technical Guide, 2nd Edition*. ASM International, 2002.
- [101] A. Strondl, S. Milenkovic, A. Schneider, U. Klement, and G. Frommeyer, “Effect of Processing on Microstructure and Physical Properties of Three Nickel-Based Superalloys with Different Hardening Mechanisms,” *Adv. Eng. Mater.*, vol. 14, no. 7, pp. 427–438, 2012, doi: 10.1002/adem.201100349.
- [102] M. M. Kirka, F. Medina, R. Dehoff, and A. Okello, “Mechanical behavior of post-processed Inconel 718 manufactured through the electron beam melting process,” *Mater. Sci. Eng. A*, vol. 680, pp. 338–346, Jan. 2017, doi: 10.1016/j.msea.2016.10.069.
- [103] D. Deng, R. L. Peng, H. Söderberg, and J. Moverare, “On the formation of microstructural gradients in a nickel-base superalloy during electron beam melting,” *Mater. Des.*, vol. 160, pp. 251–261, Dec. 2018, doi: 10.1016/j.matdes.2018.09.006.
- [104] S.-H. Sun *et al.*, “Electron beam additive manufacturing of Inconel 718 alloy rods: Impact of build direction on microstructure and high-temperature tensile properties,” *Addit. Manuf.*, vol. 23, pp. 457–470, Oct. 2018, doi: 10.1016/j.addma.2018.08.017.
- [105] E. Chauvet *et al.*, “Hot cracking mechanism affecting a non-weldable Ni-based superalloy produced by selective electron Beam Melting,” *Acta Mater.*, vol. 142, pp. 82–94, Jan. 2018, doi: 10.1016/j.actamat.2017.09.047.
- [106] H. Galarraga, D. A. Lados, R. R. Dehoff, M. M. Kirka, and P. Nandwana, “Effects of the microstructure and porosity on properties of Ti-6Al-4V ELI alloy fabricated by electron beam melting (EBM),” *Addit. Manuf.*, vol. 10, pp. 47–57, Apr. 2016, doi: 10.1016/j.addma.2016.02.003.
- [107] A. A. Martin *et al.*, “Dynamics of pore formation during laser powder bed fusion additive manufacturing,” *Nat. Commun.*, vol. 10, no. 1, Art. no. 1, Apr. 2019, doi: 10.1038/s41467-019-10009-2.
- [108] W. J. Sames V., “Additive manufacturing of Inconel 718 using electron beam melting: Processing, post-processing, & mechanical properties,” *PhD Thesis*, 2015, Accessed: May 09, 2019. [Online]. Available: <http://adsabs.harvard.edu/abs/2015PhDT.....337S>.
- [109] P. Kontis *et al.*, “Atomic-scale grain boundary engineering to overcome hot-cracking in additively-manufactured superalloys,” *Acta Mater.*, vol. 177, pp. 209–221, Sep. 2019, doi: 10.1016/j.actamat.2019.07.041.
- [110] P. G. Shewmon, “Grain boundary cracking,” *Metall. Mater. Trans. B*, vol. 29, no. 3, pp. 509–518, Jun. 1998, doi: 10.1007/s11663-998-0085-z.

## REFERENCES

- [111] P. Prabhakar, W. J. Sames, R. Dehoff, and S. S. Babu, “Computational modeling of residual stress formation during the electron beam melting process for Inconel 718,” *Addit. Manuf.*, vol. 7, pp. 83–91, Jul. 2015, doi: 10.1016/j.addma.2015.03.003.
- [112] “ASTM E562-08, Standard Test Method for Determining Volume Fraction by Systematic Manual Point Count, ASTM International, West Conshohocken, PA, 2008, [www.astm.org](http://www.astm.org).” .
- [113] C. A. Schneider, W. S. Rasband, and K. W. Eliceiri, “NIH Image to ImageJ: 25 years of image analysis,” *Nat. Methods*, vol. 9, no. 7, pp. 671–675, Jul. 2012.
- [114] M. B. Djurdjević and M. A. Grzinčić, “The effect of major alloying elements on the size of the secondary dendrite arm spacing in the as-cast Al-Si-Cu alloys,” *Arch. Foundry Eng.*, vol. Vol. 12, iss. 1, pp. 19–24, 2012.



# APPENDED PUBLICATIONS

**Paper A: Microstructure development in track-by-track melting of EBM-manufactured Alloy 718**

**Paper B: Influence of successive thermal cycling on microstructure evolution of EBM-manufactured Alloy 718 in track-by-track and layer-by-layer design**

**Paper C: Influence of build layout and orientation on microstructural characteristics of electron beam melted Alloy 718**

**Paper D: Effect of build location on microstructural characteristics and corrosion behavior of EB-PBF built Alloy 718**

**Paper E: EBM-manufactured single tracks of Alloy 718: Influence of energy input and focus offset on geometrical and microstructural characteristics**

**Paper F: Contour design to improve topographical and microstructural characteristics of Alloy 718 manufactured by electron beam-powder bed fusion technique**

**Paper G: Columnar-to-equiaxed transition in powder bed fusion via mimicking casting solidification and promoting in-situ recrystallization**

**Paper H: Tailored grain morphology via a novel double melting strategy in electron beam-powder bed fusion**



## **Tidigare avhandlingar – Produktionsteknik**

PEIGANG LI Cold Lap Formation in Gas Metal Arc Welding of Steel An Experimental Study of Micro-lack of Fusion Defects, 2013:2.

NICHOLAS CURRY Design of Thermal Barrier Coatings, 2014:3.

JEROEN DE BACKER Feedback Control of Robotic Friction Stir Welding, 2014:4.

MOHIT KUMAR GUPTA Design of Thermal Barrier Coatings A modelling approach, 2014:5.

PER LINDSTRÖM Improved CWM Platform for Modelling Welding Procedures and their Effects on Structural Behavior, 2015:6.

ERIK ÅSTRAND A Framework for Optimised Welding of Fatigue Loaded Structures Applied to Gas Metal Arc Welding of Fillet Welds, 2016:7.

EMILE GLORIEUX Multi-Robot Motion Planning Optimisation for Handling Sheet Metal Parts, 2017:10.

EBRAHIM HARATI Improving fatigue properties of welded high strength steels, 2017:11.

ANDREAS SEGERSTARK Laser Metal Deposition using Alloy 718 Powder Influence of Process Parameters on Material Characteristics, 2017:12.

ANA ESTHER BONILLA HERNÁNDEZ On Cutting Tool Resource Management, 2018:16.

SATYAPAL MAHADE Functional Performance of Gadolinium Zirconate/YSZ Multi-layered Thermal Barrier Coatings, 2018:18.

ASHISH GANVIR Design of suspension plasma sprayed thermal barrier coatings, 2018:20.

AMIR PARSIAN Regenerative Chatter Vibrations in Indexable Drills: Modeling and Simulation, 2018:21.

ESMAEIL SADEGHIMERESHT High Temperature Corrosion of Ni-based Coatings, 2018:23.

VAHID HOSSEINI Super Duplex Stainless Steels. Microstructure and Properties of Physically Simulated Base and Weld Metal, 2018:24.

MORGAN NILSEN Monitoring and control of laser beam butt joint welding, 2019:27.

ARBAB REHAN Effect of heat treatment on microstructure and mechanical properties of a 5 wt.% Cr cold work tool steel, 2019:28.

KARL FAHLSTRÖM Laser welding of ultra-high strength steel and a cast magnesium alloy for light-weight design, 2019:29.

EDVARD SVENMAN An inductive gap measurement method for square butt joints, 2019:30.

NAGESWARAN TAMIL ALAGAN Enhanced heat transfer and tool wear in high-pressure coolant assisted turning of alloy 718, 2019:31.

ADNAN AGIC, Edge Geometry Effects on Entry Phase by Forces and Vibrations, 2020:32.

ANA CATARINA FERREIRA MAGALHÃES, Thermoelectric Measurements for Temperature Control of Robotic Friction Stir Welding, 2020:33

ASHWIN DEVOTTA, Improved finite element modeling for chip morphology prediction in machining of C45E steel, 2020:34

TAHIRA RAZA, Process Understanding and Weldability of Laser-Powder Bed Fusion Manufactured Alloy 718, 2020:35





# Electron beam-powder bed fusion of Alloy 718:

## Effect of process parameters on microstructure evolution

Electron beam-powder bed fusion (EB-PBF) is an innovative additive manufacturing (AM) process, in which a metallic powder is completely melted by a high-energy electron beam. The EB-PBF process typically takes place in vacuum at high temperatures, resulting in relatively dense parts with low residual stress and material properties that are better than as-cast materials and comparable to those of wrought materials.

This research aimed to find the relationship between the manufacturing process and the microstructure of EB-PBF-built Alloy 718. To address this aim, in the first step, the microstructural evolution during building parts with different geometries were fundamentally examined. One of the major capabilities of EB-PBF is building multiple parts simultaneously. However, there was a knowledge gap concerning the effect of position and orientation (such as gap between parts on the build plate, height from the build plate, and sample location on the build plate) on the microstructural characteristics, which were explored in this study. Further, the effects of some critical machine-related parameters on the microstructural characteristics, including internal and external defects, grains, primary dendrite arm spacing, and phases, were revealed. Another aim was to develop convenient approaches by altering critical machine-related parameters for tailoring the microstructure, particularly the grain structure. The overall goal was to find the proper process window, in which parts could be built with fewer internal and external defects and develop novel approaches to tailor the microstructure.



### Paria Karimi

Received her B.Sc. degree in Production Technology from Amirkabir University of Technology - Tehran Polytechnic, Iran in 2009. She obtained her M.Sc. degree in Manufacturing Engineering at University West, Sweden in 2015. She studied the effect of the laser-powder bed fusion (L-PBF) process parameters on the microstructural characteristics of Alloy 718. Her research interests stand broadly around Additive Manufacturing Processes, Advanced Materials Characterization, Alloy Design, and Process Development.